Discrete Dynamics in Nature and Society, Vol. 2, pp. 215–242
Reprints available directly from the publisher
Photocopying permitted by license only

How and Why Do Neurons Generate Complex Rhythms with Various Frequencies?

TERESA REE CHAY[a,*] and YOUNG SEEK LEE[b]

[a]*Department of Biological Sciences, University of Pittsburgh, Pittsburgh, Pennsylvania 15260, USA;*
[b]*Department of Biochemistry, Hanyang University, Ansan, Kyung-Gi-Do, Korea*

(Received 20 May 1998)

Some neurons generate endogenous rhythms with a period of a few hundred milliseconds, while others generate rhythms with a period of a few tens of seconds. Sometimes rhythms appear chaotic. Explaining how these neurons can generate various modes of oscillation with a widely ranging frequency is a challenge. In the first part of this review, we illustrate that such rhythms can be generated from simple yet elegant mathematical models. Chaos embedded in rhythmic activity has interesting characteristics that are not seen in other physical systems. Understanding of how these neurons utilizes endogenous rhythms to communicate with each other is important in elucidating where the brain gets various rhythms and why it can pervert into abnormal rhythms under diseased conditions. Using the islet of Langerhans in pancreas as an example, in the second part of this review, we illustrate how insulin secreting β-cells communicate with glucagon secreting α-cells to achieve an optimal insulin release.

Keywords: Bursting, Spiking, Chaos, Bifurcations, Frequency modulation

1. INTRODUCTION

Neurons generate action potentials upon receiving synaptic input or external stimuli. Sometimes, the action potential appears in a form of tonic firing. Other times it appears as a burst consisting of spikes that are separated by a silent quiescent period. These rhythms are important for maintaining our daily life. For example, burst firing of 0.1–4 Hz (known as delta wave) is found during deep sleep, spindle wave of 7–14 Hz is found in the early states of sleep, and single spike firing of 20–80 Hz (gamma wave) is found during the awake state (Steriade *et al.*, 1993). This oscillatory behavior is believed to originate from a network of neurons in the thalamus and cortex (Steriade and Llinas, 1988). Each neuron involved in this network is believed to possess endogenous rhythmic activity, and its frequency is modulated by the secondary messengers (e.g., cyclic AMP) which can alter the property of the pacemaker currents (McCormick, 1992).

* Corresponding author. E-mail: trc1@vms.cis.pitt.edu

In the first part of this review, we treat rhythmic activity of three types of neurons. Our first neuron is the thalamocortical neuron. This neuron connects thalamus to cortex. Thalamus is the principal gateway to the cortex, and essentially all inputs to the cortex are relayed through the thalamus. In addition to the generation of the rhythms of sleep, thalamus is involved in the pathological spike and wave of absence epilepsy (Steriade *et al.*, 1993). Our second neuron is the pyramidal neuron in hippocampus. This neuron is of great interest to neuroscientists since a single neuron can generate a variety of interesting electrical behaviors (Wong and Prince, 1981). In addition, groups of hippocampal neurons can generate synchronized epileptiform oscillations (Traub *et al.*, 1991). To those readers who are not familiar with neuroscience, we include Fig. 1 which illustrates the structure of the central nervous system. Our third neuron is the bursting neurons of molluscan ganglion. Gastropod molluscs have the largest and most accessible cell body of the animal kingdom. Because of these, they are particularly suited to study learning and memory. Some of the neurons in this family have the ability to burst when isolated from their neighboring cells (Lotshaw *et al.*, 1986).

In Fig. 2A, we show the intracellular recordings made on the thalamocortical neuron (TCN). This figure is retouched from Fig. 3 of Nunez *et al.* (1992). As shown in the top frame, TCN gives rise to oscillations when the membrane potential is around $-57\,\text{mV}$. This oscillation has a form of spindle wave consisting of a high-amplitude spike mixed with small-amplitude oscillations. When the potential is lowered to $-65\,\text{mV}$ by the application of a hyperpolarization current (first arrow), the spindle oscillation persists. The feature associated with the spindle oscillation can be seen more clearly

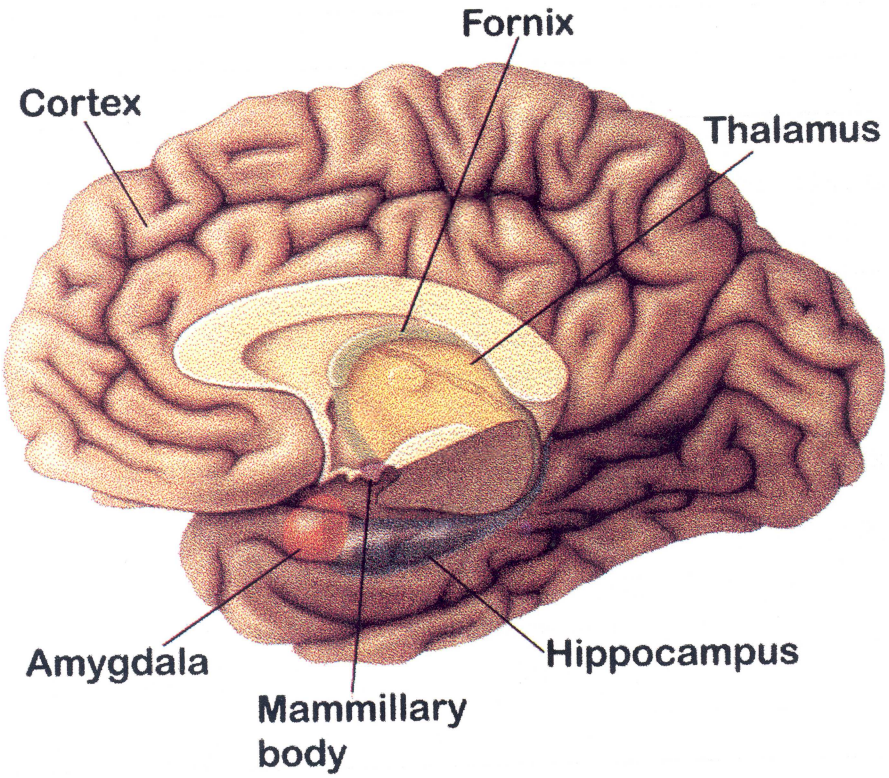

FIGURE 1 The central nervous system showing the location of hippocampus, cortex, and thalamus. (See Color Plate I.)

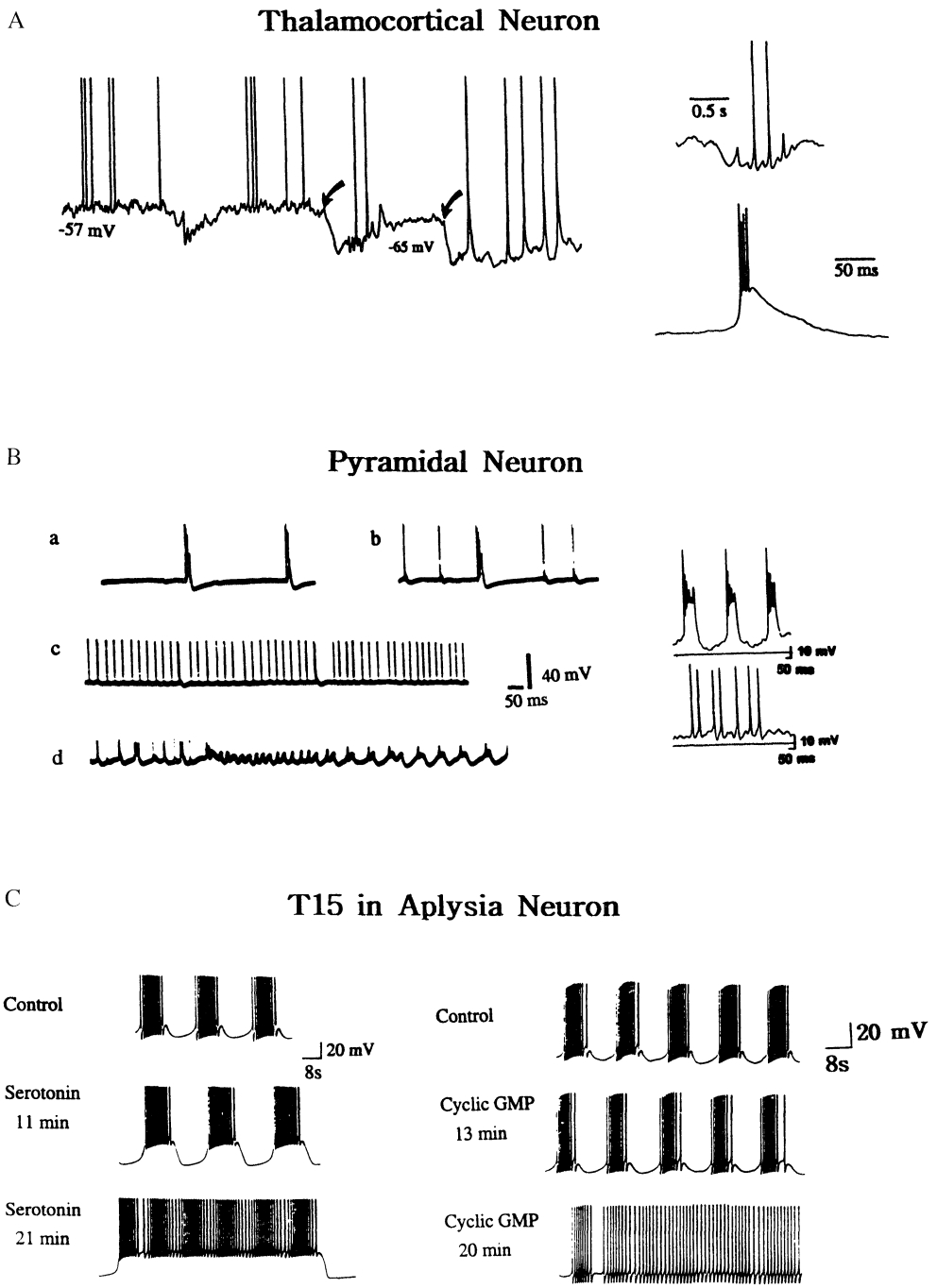

FIGURE 2 Endogenous bursting generated by thalamocortical neurons (frame A), pyramidal neurons (frame B), and T15 neuron of *Aplysia* of mollusc family (frame C). Note that the former two bursters are fast bursters with a bursting period of few hundred milliseconds, while the later is a slow burster with a period of few tens of seconds. In frame A, a hyperpolarizing current is applied at the first arrow, and a stronger hyperpolarization current is applied at the second arrow. The insets show spindle (left) and delta (right) waves. In frame B, a depolarization current is increased from trace a to b, to c, and finally to d. The top inset shows bursting in an expanded scale, and the bottom inset shows repetitive spiking. In frame C, serotonin is applied steadily on the left, and cyclic GMP analog is applied steadily on the right.

in an expanded scale on the upper right trace. Further hyperpolarization (second arrow) brings the membrane potential to −80 mV, and this in turn induces delta oscillation. The delta oscillation consists of fast spikes that appear on the top of a slow wave, as can be seen more clearly in an expanded scale on the lower right trace.

In Fig. 2B, we show the recording of pyramidal neurons in the hippocampus. This figure is retouched from Fig. 2 of Wong and Prince (1981). As shown in trace a, the pyramidal neurons with resting potentials of less than −65 mV burst spontaneously. The burst typically consists of groups of 2–10 spikes separated by a long duration of post-burst hyperpolarizations (0.5–2 s). This can be seen more clearly in an expanded scale on the right. When the membrane potential is depolarized by a steady depolarizing current, the frequency of burst firing increases to a maximum of not more than 5 Hz (see trace b). On further depolarization, the spontaneous activity consists of a mixture of solitary spikes and burst firing (see trace c). At a more depolarized level, only single spikes persist (see the bottom right trace). Finally, the neuronal response changes from trains of fast spikes to long duration slow spikes with an amplitude of about 20 mV (see trace d).

In Fig. 2C, we have displayed the bursting behavior of the R15 neurons in the abdominal ganglion of the marine mollusc *Aplysia* californica (hereafter referred to as the mollusc neuron, MLN). This figure is retouched from Figs. 1 and 9 of Lotshaw *et al.* (1986). As shown in the left frame, serotonin enhances the interburst hyperpolarization at first (middle trace), but a longer application of serotonin induces continuous spiking (bottom trace). A structure similar to this has been observed in the presence of cyclic GMP analog guanylylimiododiphosphate (see the right frame). This transformation is believed to be induced by protein kinase A that acts on several different types of ion channels. This kinase is activated by cyclic adenosine monophosphate (cAMP), which is produced when serotonin binds to a receptor involved in the adenylate–cyclase transduction pathway.

To reiterate, TCN and the hippocampal pyramidal neuron (PYN) are the neurons in the central nervous system. These neurons are fast bursters whose burst period is about few hundred milliseconds. On the other hand, the *Aplysia* T15 neurons are the neurons in mollusc family, whose soma is larger than any known neuron. They are slow bursters with a periodicity of a few tens of seconds. In Sections 2 and 3, we explain how a minimal mathematical model can be derived for rhythmic activity of these neurons. In Section 4, we demonstrate that complex rhythms with seemingly different periodicity may arise from these mathematical models. In Sections 5–8, we display various dynamic tools that can unravel complex structures embedded in these neuronal models. In Section 9, taking the islet cells in the mouse pancreas as an example, we show how a network of excitable cells can utilize endogenous rhythmic activity in order to achieve their physiological functions. Section 10 summarizes the present review and discusses a future outlook.

2. MODEL

As shown in Fig. 3, a typical neuron consists of the cell body (soma), dendrites which receive information from the presynaptic neuron, and the axon

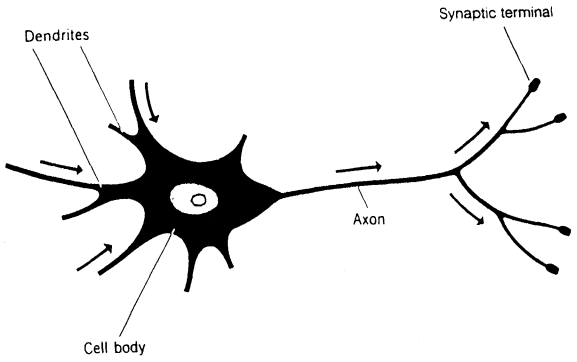

FIGURE 3 A schematic representation of a neuron which consists of cell body (soma), dendrites where the neuron received information from the synaptic terminal, and axon where the action potential is transmitted to the synaptic terminal, and synapse where the neurotransmitter is released.

which carries impulses to the postsynaptic cell. The axon terminates at specialized structures called synapses. Modeling the whole structure of the neuron is an impossible task, since there are so many unknowns. Moreover, it defeats the purpose of modeling; the essence of mathematical modeling is to explain complex phenomena (e.g., Fig. 2) by picking up only the main events. To explain endogenous rhythmic activity, our group has developed a one-compartment neuronal model (Chay, 1983; 1984; 1985a; 1990a,b; 1993a,b; 1996a,b; Chay and Fan, 1993; Chay and Cook, 1988; Chay and Lee, 1990; Chay *et al.*, 1995). This compartmental model is a model that lumps the dendritic membrane with the soma, and all the inputs are delivered to the lumped membrane. This simplified model helps one understand the essential features that are required for endogenous rhythms. In addition, a one-compartment model is useful as building block for the construction of network models, which can be used for the study of epilepsy, schizophrenia and Alzheimer disease.

The TCN model described in this paper is adopted from Chay and Fan (1993). In this model, the plasma membrane contains a voltage-activated, low-threshold Ca^{2+} channel (T-type) that inactivates in a voltage-dependent manner. In addition, the model contains Hodgkin–Huxley type Na^+ and K^+ channels and a leak current (Hodgkin and Huxley, 1952). The low-threshold T-type current I_{Ca} activates first, and this activation in turn gives rise to a higher threshold Na^+ current I_{Na}. Activation of I_{Na} in turn activates a delayed rectifying K^+ current $I_{K(DR)}$, that leads to spike activity. Thus, I_{Ca} is a pacemaker current that generates bursting in TCN.

The PYN model is an unpublished result of Chay and Lee, where a mixed inward current in the three-variable model of Chay (1985a) is separated by Na^+ and Ca^{2+} currents. This neuron contains a Ca^{2+}-sensitive K^+ channel [K(Ca) channel], in addition to all the channels in TCN. Unlike the Na^+ and Ca^{2+} channels in TCN, however, the Na^+ channel in PYN is a low-threshold channel, while the Ca^{2+} channel (L-type) is a high-threshold channel that does not inactivate. In this cell, the Na^+ current activates first, and this in turn activates the higher threshold Ca^{2+} current. In PYN, $[Ca^{2+}]_i$ is a dynamic variable that depends on influx of extracellular Ca^{2+} from outside through the calcium channel and efflux of Ca^{2+} via the Ca^{2+}-pump. During the spiking Ca^{2+} accumulates slowly. This accumulation in turn activates $I_{K(Ca)}$, leading to the termination of the plateau. Thus, $I_{K(Ca)}$ is a pacemaker current that generates bursting in PYN.

There are several models formulated for MLN (Chay, 1983; 1990a; 1996a,b), but the model described in this paper (Chay, 1996a) is attractive in that it depicts only a minimal feature of MLN. In this model, the bursting is due to the participation of the endoplasmic reticulum (ER), which releases luminal Ca^{2+} by the calcium-induced calcium release (CICR) mechanism (Berridge, 1991). The calcium concentration in ER, $[Ca^{2+}]_{ER}$, modulates a voltage-independent Ca^{2+} channel in the plasma membrane known as a CRAC (calcium release activated current) channel (Hoth and Penner, 1992). In addition, this model contains a voltage-dependent Ca^{2+} channel, a delayed rectifying K^+ channel, and a leak current. In this model, $[Ca^{2+}]_i$ is a fast dynamic variable that activates the calcium-releasing channel (CRC) in the ER. On the other hand, $[Ca^{2+}]_{ER}$ is a slow dynamic variable that modulates I_{crac}, the pacemaker current.

To recapitulate, these models utilize three distinct mechanisms in order to burst – the first model utilizes an oscillating T-type Ca^{2+} current, the second model utilizes a Ca^{2+}-sensitive K^+ channel that is modulated by oscillating intracellular Ca^{2+} concentration, and the third model utilizes a voltage-independent Ca^{2+} channel that is modulated by the calcium concentration in the ER.

3. MATHEMATICAL FORMULATION

The change of membrane potential with time in TCN can be described by the following electrical

circuit equation (Hodgkin and Huxley, 1952):

$$C_m \frac{dV}{dt} = -\sum_i I_i + I_{app}, \quad (1)$$

where the sum runs over all the ionic components in the plasma membrane, and I_{app} is an externally applied current. The gating variables that appear in the current components (see Appendix I) can be described by first-order kinetics:

$$\frac{dy}{dt} = \frac{y_\infty - y}{\tau_y}, \quad (2)$$

where y_∞ and τ_y are the gating variable y at its steady state and the relaxation time constant, respectively, and these variables are expressed by

$$y_\infty = \frac{1}{1 + \exp((V_y - V)/S_y)} \quad (3)$$

and

$$\tau_y = \lambda_y \left\{ \exp\left(a_y \frac{V_y - V}{S_y} \right) + \exp\left((a_y - 1) \frac{V_y - V}{S_y} \right) \right\}^{-1}, \quad (4)$$

where V_y is the voltage at the half maximal point of the y_∞ curve, S_y is the slope at $V = V_y$, λ_y is an inverse of the maximal τ_y, and a_y determines how τ_y depends on voltage (for example, $a_y = 0.5$ makes τ_y a bell shape as an increasing function of V).

In PYN, $[Ca^{2+}]_i$ can be described by

$$\frac{d[Ca^{2+}]_i}{dt} = -\phi I_{Ca} - k_{Ca}\left([Ca^{2+}]_i - [Ca^{2+}]_r \right), \quad (5)$$

where ϕ is the factor that converts the electromotive force to the concentration gradient, I_{Ca} is the Ca^{2+} current, k_{Ca} measures Ca^{2+}-ATPase activity in the plasma membrane, and $[Ca^{2+}]_r$ is the intracellular calcium concentration at the resting potential.

In MLN, $[Ca^{2+}]_{ER}$ is a dynamic variable described by the following equation:

$$\frac{d[Ca^{2+}]_{ER}}{dt} = -\rho J_{ER} = \rho \left\{ k_{pump} \frac{[Ca^{2+}]_i^2}{K_p^2 + [Ca^{2+}]_i^2} [Ca^{2+}]_i - k_{rel} \frac{[Ca^{2+}]_i}{K_r + [Ca^{2+}]_i} \times \left([Ca^{2+}]_{ER} - [Ca^{2+}]_i \right) \right\}, \quad (6)$$

where J_{ER} is a net flux of $[Ca^{2+}]_{ER}$, ρ is a measure of the fraction of free Ca^{2+} in the ER, the first term inside the curly bracket is intracellular Ca^{2+} pumped into the ER by the sarcoplasmic/endoplasmic calcium ATPase (SERCA), and the second term is due to Ca^{2+} released from CRC via the CICR mechanism. In addition, Eq. (5) is modified such that J_{ER} is added to account for the net increase of $[Ca^{2+}]_i$ due to the ER, and ϕI_{crac} is subtracted to account for the increase of Ca^{2+} due to the CRAC channel. For more detail see Chay (1996a).

4. TIME SERIES

Figures 4A and B show the time series simulated from the TCN models. The numbers at the right margin show the strengths of I_{app} used for the computation. The top frame of Fig. 4A shows interspike intervals (ISI) in milliseconds as a function of I_{app}. ISI includes only the interval between the high-amplitude spikes, not the low-amplitude oscillation seen in the time series. Likewise, the top frame of Fig. 4B shows ISI as a function of I_{app}.

As shown in Fig. 4A, TCN is quiescent at the resting potential of -60 mV (taking $I_{app} = 2.6\,\mu A/cm^2$ as a base line since this current can be absorbed into a leak current). When a depolarization current of $20.7\,\mu A/cm^2$ is applied to this neuron, the model gives rise to tonic oscillation (i.e., repetitive firing). When a hyperpolarization current of $2.254\,\mu A/cm^2$

is applied, a low-amplitude oscillation grows gradually, and this leads to a large-amplitude spike. Note that the spike occurs at a regular interval (i.e., every seventh time). When a hyperpolarization current is increased further, a spike appears more often (i.e., every fourth at 2.12, every third at 2.02, and every other at 1.85). Finally at $I_{app} = 1.34\,\mu A/cm^2$, the low-amplitude oscillations disappear completely and single spike remains (referred to as 1-spike bursting). Between the regular spindle

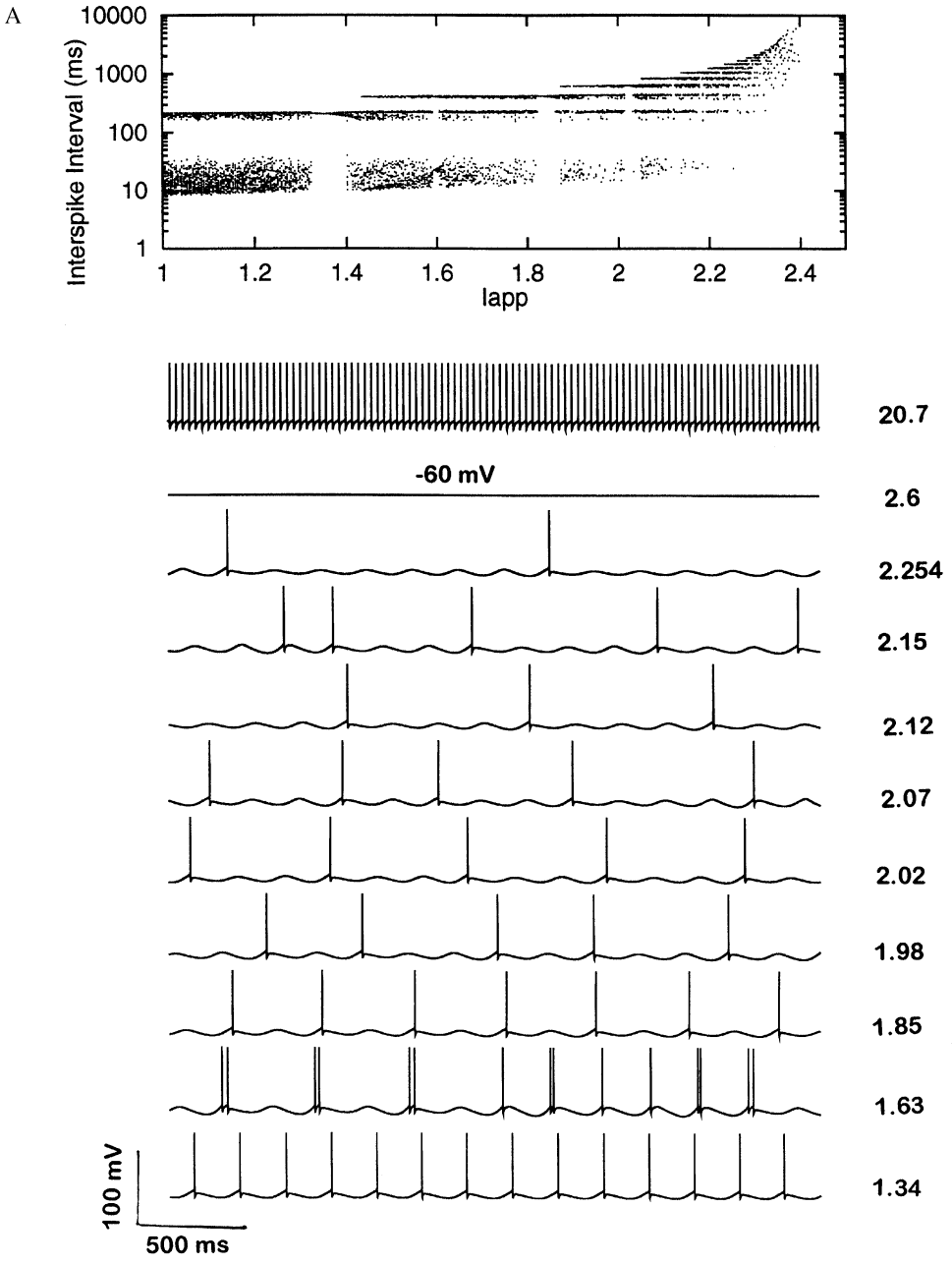

FIGURE 4(A)

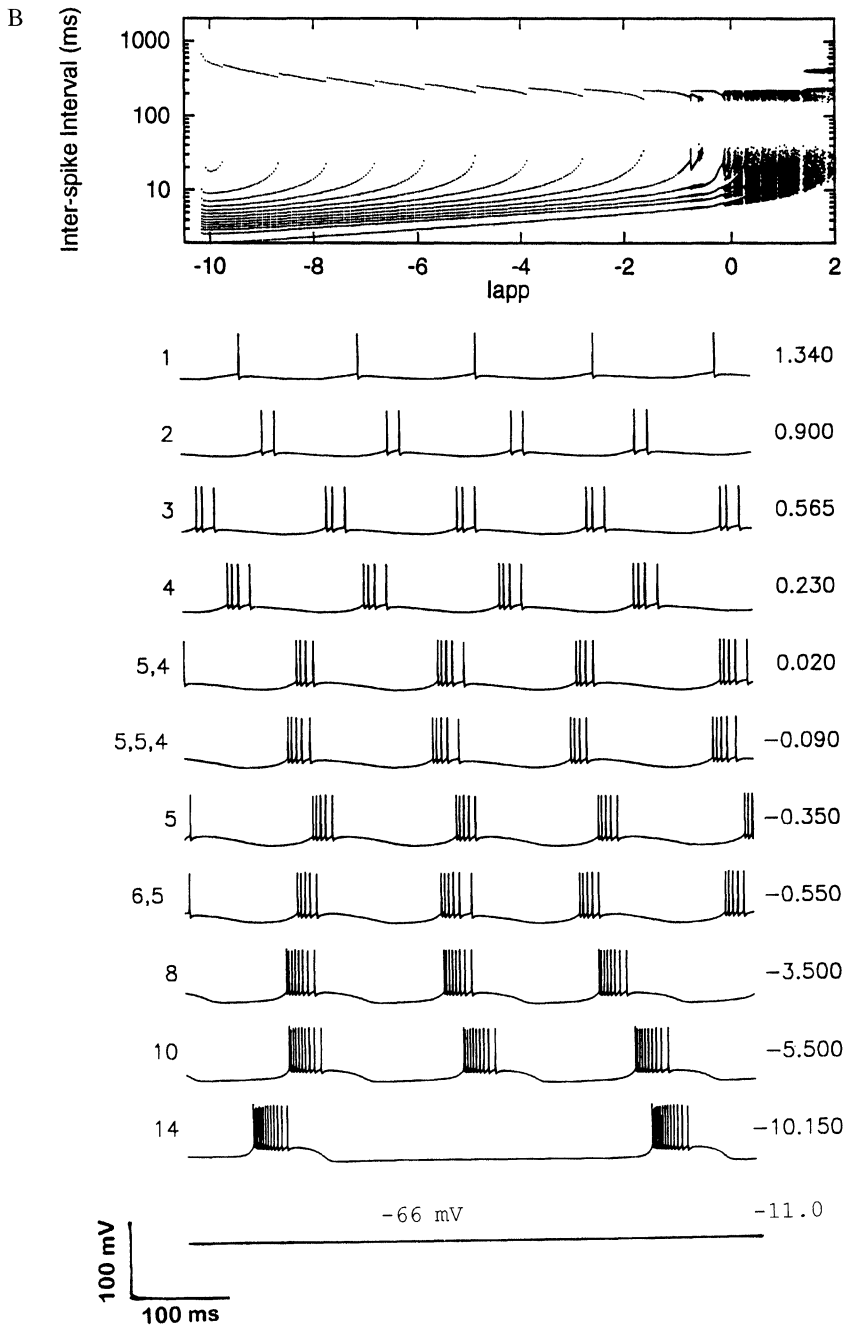

FIGURE 4(B)

FIGURE 4 Time series generated by the thalamocortical neurons as a hyperpolarization current I_{app} is increased from the top to the bottom. A: Low- and high-amplitude oscillations and chaos are generated as I_{app} decreased from the top to the bottom. The values shown on the right are the strength of I_{app} in $\mu A/cm^2$. B: Bursting exhibited by this neuron as I_{app} is decreased further. The labels on the left represent the number of spikes per burst. For example, (5,4) represents bursting consisting of an alternating sequence of 4- and 5-spikes, and (5,5,6) represents the bursts consisting of an alternating sequence of 5-, 5-, and 6-spikes. The top frames of A and B show the interspike intervals (ms) from Fig. 7 in an expanded scale.

oscillations resides chaos where a large-amplitude spike appears chaotically (see the traces generated by $I_{app} = 2.15$, 2.07, and 1.63). Between one low-amplitude (third trace from the bottom) and two low-amplitude oscillations (the fifth trace from the bottom) appears an alternating sequence of one low-amplitude oscillation, spike, and two low-amplitude oscillations (see the fourth trace from the bottom). This complex pattern can be seen more clearly by the ISI plot on the top frame.

When the strength of a hyperpolarization current is increased further (see Fig. 4B), the 1-spike bursting transforms to 2-spike bursting, 2 to 3, until 15-spike bursting appears. Beyond the 15-spike bursting the cell transforms to another quiescent resting state of -66 mV. Note that in some regions two types of bursting coexist, e.g., 4- and 5-spike burstings appear in an alternating order at $0.020\,\mu A/cm^2$; bursts consisting of 5-, 5-, 4-spikes appear in a consecutive order at $-0.090\,\mu A/cm^2$, and an alternating order of 6- and 5-spike burstings appears at $-0.55\,\mu A/cm^2$. Between these alternating burstings there appear chaos. The ISI plot on the top frame reveals all the chaotic regimes that exist between -0.350 and 1.340.

The bursting exhibited by PYN is relatively simple, and this is shown in Fig. 5. Here, the numbers on the right margin indicate I_{app} used for the simulation. As I_{app} increases, a spike is added one by one starting from five spikes until seven spikes appear. Beyond this bursting scenario, repetitive firing resides such that its frequency increases as the strength of I_{app} increases. During the bursting $[Ca^{2+}]_i$ accumulates (see the

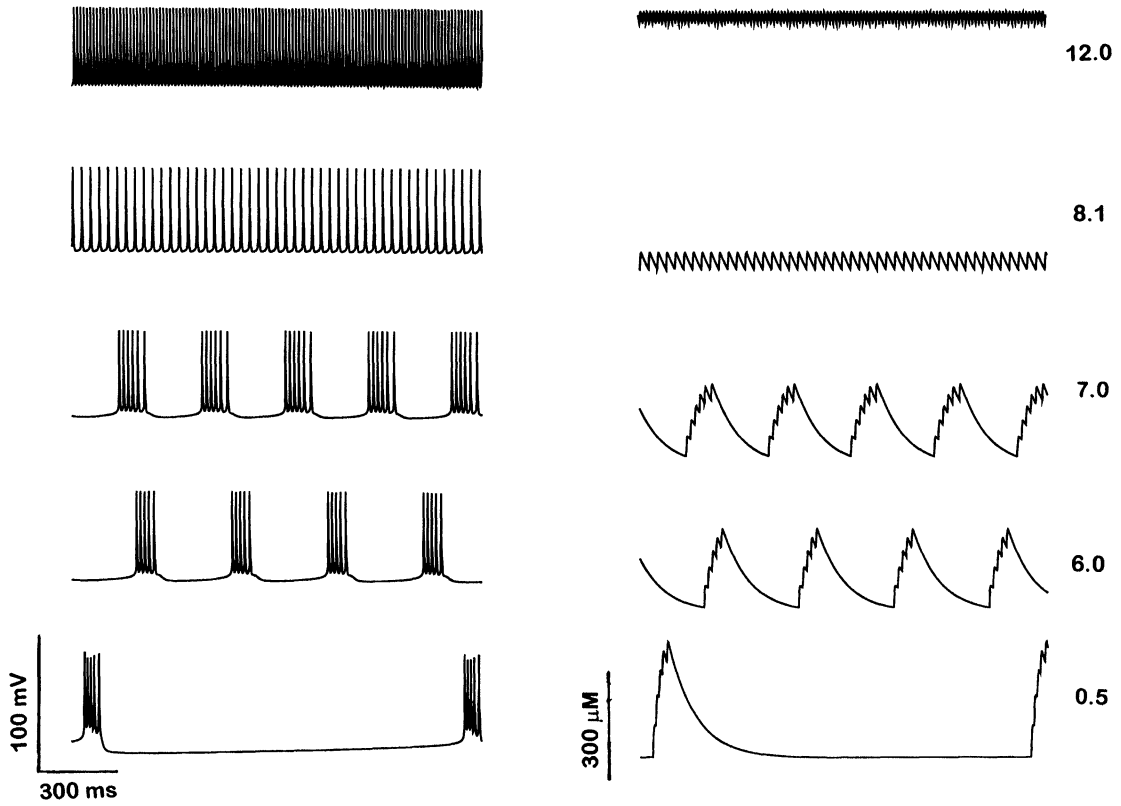

FIGURE 5 Time series of the membrane potential (left) and $[Ca^{2+}]_i$ (right) of the pyramidal neuron as a steady depolarization current, I_{app}, is increased from the top to the bottom. The values of I_{app} (in unit of $\mu A/cm^2$) are listed on the left. Note that the burst generated by PYN is frequency modulation in that the shape remains the same while the frequency increases drastically as I_{app} increases.

right frame), and this accumulation in turn activates the K(Ca) channel. This simulation is similar to that generated by the excitable models of Plant (1981), Chay (1983; 1984; 1985a) and the model of Traub *et al.* (1991) using their 19-compartment model for the hippocampal pyramidal neurons. Note that as I_{app} increases the burst-to-burst interval changes dramatically, while the duration and amplitude of a spike remain about the same. This type of bursting is known as frequency modulation.

As shown in Fig. 6, in MLN the bursting starts with 1-spike bursting (see the bottom trace). The spikes are added one by one, as I_{app} increases. Beyond the 6-spike bursting resides tonic firing. Note that $[Ca^{2+}]_i$ is a fast dynamic variable that follows closely the electrical bursting. It, however, differs from electrical bursting such that $[Ca^{2+}]_i$ rises rapidly during the upstroke of V, spikes are generated during the plateau, then $[Ca^{2+}]_i$ falls slowly during the repolarization (until the next upstroke of membrane potential is initiated). This slowly falling phase of $[Ca^{2+}]_i$ is due to a slow release of the luminal Ca^{2+} from the ER (even after the Ca^{2+} channel closes). In contrast to the $[Ca^{2+}]_i$ oscillation, $[Ca^{2+}]_{lum}$ is a slow dynamic variable that accumulates during the plateau, and this accumulation in turn inactivates I_{crac}. Sometimes, bursting becomes chaotic as seen in the fourth trace from the top.

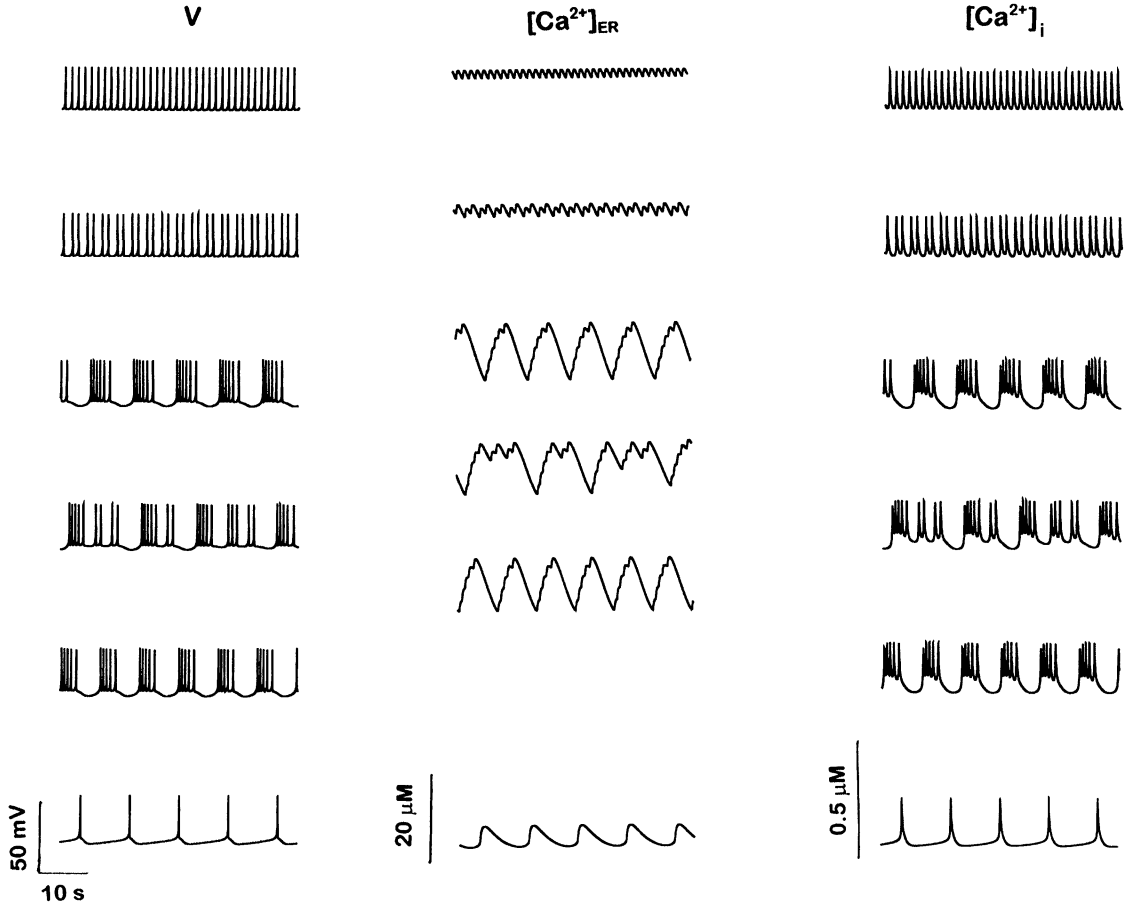

FIGURE 6 Time series generated by the mollusc neuron, where V (left), $[Ca^{2+}]_{ER}$ (middle) and $[Ca^{2+}]_i$ (right) are shown in an increasing function of I_{app}. From the top to the bottom I_{app} used for the computations are 5.0, 3.0, 2.0, 1.0, 0.0, $-18.0\,\mu A/cm^2$. Note chaos in the fourth trace and doublets in the second trace.

5. BIFURCATION DIAGRAMS

Bifurcation diagram is a diagram that reveals the dynamic structure as a function of a bifurcation parameter. With this diagram, it is insightful to gain information on how the bursting transforms to tonic firing as I_{app} increases. Bifurcation diagrams shown in Figs. 7–9 are constructed by solving the dynamic equations in Section 3. Here, I_{app} increased incrementally and automatically by a small step starting from a low value of I_{app}. The ISI (top frames) were obtained by first recording the time, T_n, as the upstroke of the nth spike crosses $V = V^*$. After collecting all T_n's, ISI were computed by subtracting T_n from T_{n-1}. The bottom frame shows a bifurcation structure of the slowest dynamic variable (e.g., f in TCN). These values were obtained by recording the value of the slowest dynamic variable at the time that the upstroke of V crosses the $V = V^*$ line. To ensure that only the values at the limit cycle are included, we threw away the first few hundred cycles. For TCN V^* is taken to be -30 mV, for PYN -10 mV, and for MLN -20 mV. Note that ISI is in units of milliseconds for TCN and PYN whereas it is in unit of seconds for MLN.

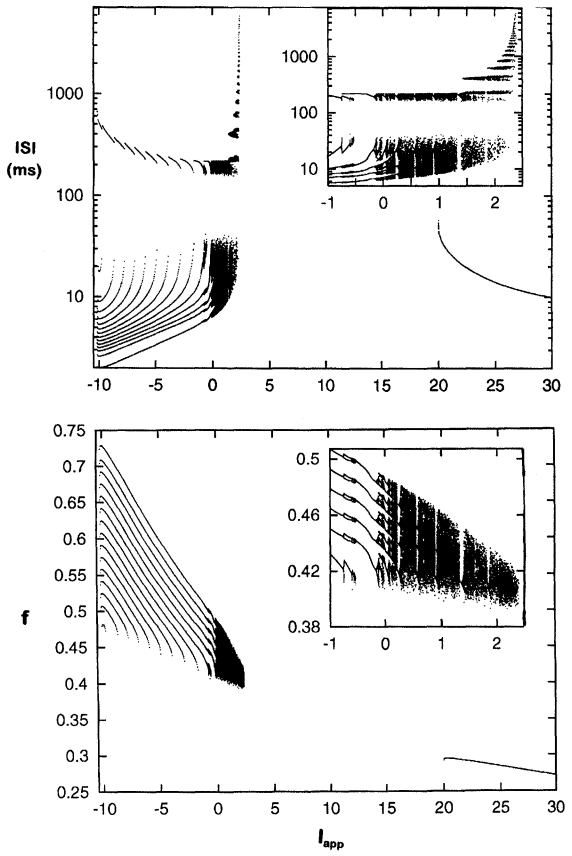

FIGURE 7 Bifurcation diagram for the thalamocortical neuron showing the interspike interval (top) and the inactivation variable of I_{Ca} (bottom) as a function of I_{app}. This diagram and subsequent two diagrams were constructed by solving the differential equations given in Section 3. ISI and f were obtained whenever the upstroke of a spike crosses the $V = -30$ mV plane.

As shown in Fig. 7 for TCN, a spike is reduced one by one starting from the 15-spike bursting. Doublets appear as the 6-spike bursting transforms to the 5-spike bursting. This doublet corresponds to the time series seen in the eighth trace from the top of Fig. 4B, where the 5- and 6-spike burstings appear in an alternating order. Between the 5- and 4-spike burstings, one finds more complex rhythms. First, a period-doubling scenario arises where the 5-spike bursting appears in doublets. Then, the period-doubling sequence ends with a sequence consisting of 5-, 5- and 4-spike burstings. How the sequence alternates can be seen more clearly from the sixth frame from the top of Fig. 4B. This alternating bursting transforms to another alternating of 4- and 5-spike burstings. The time series of 5- and 4-bursting is displaced in the fifth trace of Fig. 4B. Chaos exists between these two alternating sequences. Then, the 5- and 4-spike burstings eventually transform to 4-spike bursting by passing through another chaotic regime. The sequence similar to this appears when the 4-spike bursting transforms to the 3-spike bursting, the 3- to 2-spike bursting, and finally to the 1-spike bursting. Beyond the 1-spike bursting lie spindle-like oscillations as shown in Fig. 4A, where low-amplitude oscillations preceed a high-amplitude spike. After passing through the resting state, the cell exhibits tonic repetitive firing.

The ISI of Fig. 7 indicates how fast TNC fires as I_{app} increases. Here, the upper line is the burst-to-burst interval, and the condensed lines in the lower part are the spike-to-spike intervals (i.e., low-amplitude oscillation is not included). As I_{app} increases, a delta wave of 1–5 Hz appears at first, and it remains there until the cell enters a spindle-type regime. In the spindle-type regime (I_{app} equals about 1.4–2.3), the frequency of the spike-to-spike interval ranges anywhere between 0.1 and 10 Hz (depending on how chaotically the spike rides on low-amplitude oscillations). Spindle chaos is not utter chaos but has several distinct bands (see also the top frame of Fig. 4A). In the tonic firing regime, the frequency increases from about 10 to 100 Hz (gamma wave) when I_{app} is increased by 1.5-fold (see the right branch of Fig. 7).

The bifurcation structure of PYN is rather simple as shown by Fig. 8. In the upper line of the top frame is the burst-to-burst interval, while the condensed lines of the lower part are the spike-to-spike interval. A period-adding sequence starts with 5-spike bursting, which leads to 6-spike bursting, and then to 7-spike bursting, before entering a repetitive firing mode. Note that the frequency of bursting increases exponentially from about 0.2 to 10 Hz. Also, $[Ca^{2+}]_i$ increases drastically by nearly 100-fold during this period. Chaos does not appear in this diagram.

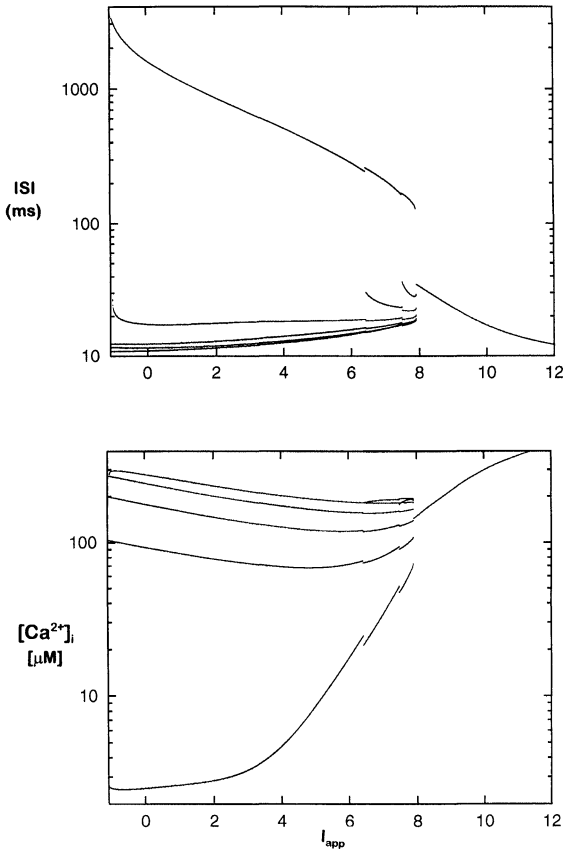

FIGURE 8 Bifurcation diagram for the pyramidal neuron showing the interspike interval (top) and $[Ca^{2+}]_i$ (bottom) as a functions of I_{app}. The ISI and $[Ca^{2+}]_i$ were collected whenever the upstroke of V passes -10 mV. Note that the bursting period (the top line in ISI) decreases exponentially while the number of spikes remains almost constant (the number of spikes can be found from the number of lines in $[Ca^{2+}]_i$).

As in PYN, MLN also starts with a period-adding sequence (i.e., 1-, 2-, 3-, 4-, 5- and 6-spikes), see Fig. 9. But unlike PYN, it ends with an inverse period-doubling route. Chaos appears in the region where a new spike is added, and the region in which chaos resides becomes wider and more complex as more spikes are added. Chaos that exists in each of the transition regimes is not simple regions of utter chaos, but there are several regular periodic states embedded in each of these chaotic regimes (Chay, 1996a).

Let us examine closely how chaos arises as one moves from the right to the left of this diagram. The right-most chaotic regime contains very complex structure. First, the route from order into chaos follows the Feigenbaum diagram of the period-doubling scenario (Feigenbaum, 1973). Out of repetitive spiking two branches bifurcate (period-2), out of these branches two branches bifurcate again (period-4), and then two branches bifurcate out of each of these again (period-8). We can follow the bifurcating tree up to period-16; afterwards spiking-chaos sets in (Chay, 1984; Chay *et al.*, 1995; Chay and Rinzel, 1993). After passing through the spiking-chaos, crisis transition (Grebogi and Ott, 1983) sets in, where spiking-chaos suddenly transforms to bursting-chaos. Even within the spiking-chaotic regime, there arises a

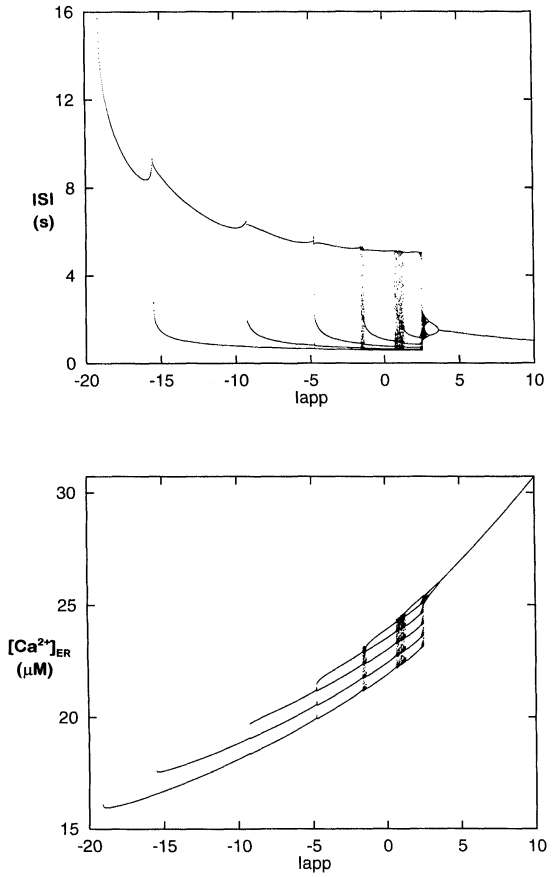

FIGURE 9 Bifurcation diagram for the mollusc neuron showing how a period-adding series starts and ends as I_{app} increases. The ISI (top) and $[Ca^{2+}]_{ER}$ (bottom) were collected whenever the upstroke of V passes -20 mV.

crisis transition, demonstrating the fractal nature of chaos. In the bursting-chaotic regime, we see a variety of beautiful structures. There exist six bands resulting from points not being uniformly distributed over this chaotic regime. The system ends with regular bursting after passing through an inverse period-doubling route (where each of six branches inversely bifurcates). Similar patterns are seen when 6-spike bursting transforms to 5-spike bursting, 5- to 4-spike bursting, 4 to 3. But the pattern becomes less complex as the spike is reduced each time. This bifurcation structure was first observed in a three-variable model of Chay (1985a, reviewed in Chay *et al.*, 1995).

6. AUTO ANALYSIS

Although the bifurcation analysis approach in Section 5 gives detailed information on the bursting regime, it does not give information of where the periodic state starts, where it ends, and whether multiple stable branches coexist in the bifurcation diagram. This information is provided by AUTO analysis (Doedel, 1981; Doedel and Kernevez, 1986; Doedel *et al.*, 1991a,b; 1997). In addition, the role of the key channels in these neurons can be seen more clearly using AUTO analyses. Figures 10–12 are the bifurcation diagrams obtained using AUTO for TCN, PYN, and MLN, respectively. In these figures, stable steady states (SSSs) are drawn by the solid green line and unstable steady states (USSs) by the same color in dashes. Two distinct periodic branches can be seen in these figures; a spiking branch on the right and a bursting branch on the left. The spiking branch where tonic firing resides is seen in the blue color with the stable periodic state (SPS) by the solid line and the unstable period state (UPS) by the dashes. The bursting branch is drawn by pinks and grays. The grays came from AUTO, and the pink dots came from the dynamic solution (whenever AUTO could not connect this branch).

The top frame of Fig. 10 reveals how the maximum and minimum membrane potentials of TCN change as I_{app} increases. Note that in the spiking branch two stable states, SPS and SSS, coexist. This means that the repetitive tonic firings seen in the top trace of Fig. 4A are very susceptible to noise, such that a small perturbation can make a firing cell to a quiescent depolarized cell, and vice versa. Note also in the region between HB (Hopf bifurcation) = 22.3166 and LP (limit point) = 23.31332, two SSSs coexist – stable repolarized and depolarized states. From LP = 23.31332 to HB = 22.3166, three states coexist – repolarized, firing, and depolarized states.

To gain further insight into the role that each channel plays, we plotted a bifurcation diagram when I_{Ca} is non-oscillatory, i.e., $d = d_\infty$ and $f = f_\infty$ (the middle frame) and that when I_{Na} is absent

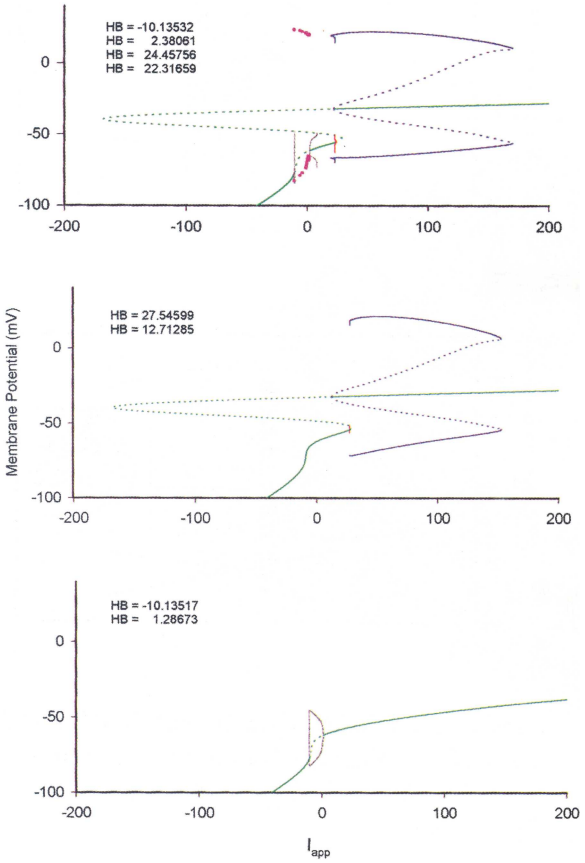

FIGURE 10 AUTO plot showing the membrane potential vs. I_{app} for the thalamocortical neuron. The top frame was obtained using the five dynamic variables (d, f, h, n, and V), the middle frame was obtained using three dynamic variables (h, n, and V) by setting d and f at their steady state values, and the bottom frame was obtained by setting $I_{Na}=0$. Here, the solid green lines are stable steady states and the dashed greens are unstable steady states. The blue envelope is a spiking branch (solid is stable and dashes are unstable). The pink circles on the top frame were obtained by solving the dynamic equations. In the top two frames, the limit points of the steady state occur at -167.9530 and 29.00959. In the top frame, the periodic limit points are located at 23.31332 and 170.04882, while in the middle frame these points are located at 27.5246 and 152.9140. HBs are listed in the figure. (See Color Plate II.)

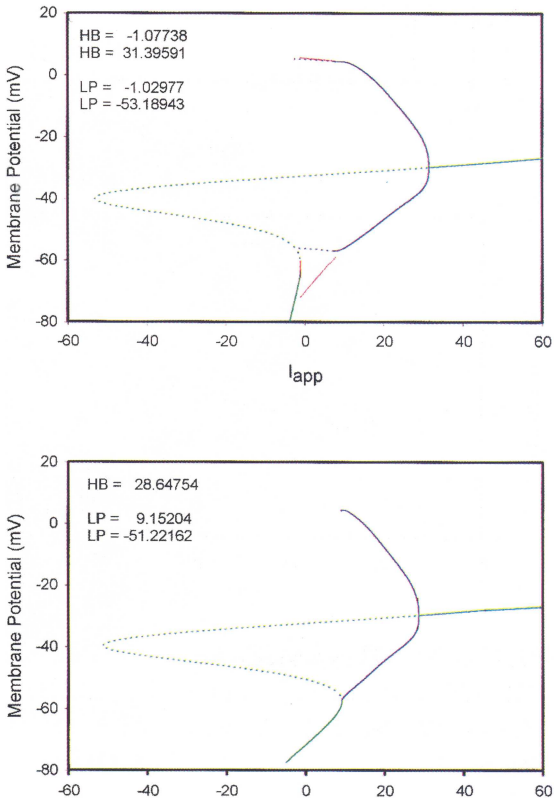

FIGURE 11 AUTO plot showing the membrane potential vs. I_{app} for the pyramidal neuron. In the bottom frame, the gating variable (p_∞) of $I_{K(Ca)}$ is fixed at $300/(K_{KC}+300)$. In the top and bottom frames, the green lines represent steady state branches and blues lines represent spiking envelopes. In the top frame the pink solid line was obtained using the dynamic solution, since AUTO was unable to continue in the bursting regime. (See Color Plate III.)

(bottom frame). As seen in the bottom frame, in the absence of I_{Na}, I_{Ca} can generate a low-amplitude oscillation, which overshoots and undershoots the steady state line (dashed green). If I_{Ca} is not oscillatory (as seen in the middle frame) the bursting branch completely disappears, and there remains the spiking branch. Note that the spiking branch in the top frame is almost identical to that in the middle frame. This implies that tonic firing is exclusively controlled by three currents, I_{Na}, I_K, and I_{leak} and the bursting is generated by the oscillatory I_{Ca}.

How important is the I_{Ca} oscillation to the genesis of bursting can be evidenced by the bottom frame. When I_{Ca} is oscillatory, the membrane potential overshoots to a level that is higher than its steady state value, and this depolarization causes activation of the Na^+ current. That is, without this depolarization, I_{Na} cannot be activated. Activation of I_{Na} leads to the bursting.

The bifurcation structure of PYN is revealed by the top frame of Fig. 11. There are two HBs in this

frame. The periodic branch that starts from the right HB is a spiking branch where tonic firing resides. The UPS starts from the left HB and terminates when it approaches the HCO. A new bursting branch that starts from this point is shown by a pink line. This pink line was obtained by the dynamic solution. To show why $I_{K(Ca)}$ is a pacemaker current that gives rise to bursting, we displayed in the bottom frame a bifurcation structure of PYN when $I_{K(Ca)}$ is non-oscillatory. $I_{K(Ca)}$ was made non-oscillatory by fixing the gating variable p_∞ at $300/(K_{KC}+300)$. Compare the top frame with the bottom frame. Note that the left HB disappears and consequently the bursting branch disappears completely when $I_{K(Ca)}$ becomes non-oscillatory.

The role that CRAC plays on the bursting for MLN can be seen by comparing the top and bottom frames of Fig. 12. The top frame shows a bifurcation structure when I_{crac} is oscillatory and the bottom frame when it is non-oscillatory. Here, I_{crac} was made non-oscillatory by fixing p_∞ at $K_{crac}\cdot/(K_{crac}+50)$. Note that the spiking branch (blue) appears both on the top and bottom frames, while the bursting branch (gray + pink) appears only on the top frame. The pink was obtained using the dynamic solution since AUTO was unable to continue this part of bursting branch. The steep change seen in the lower part of the bursting branch is where the spike is added, starting from 1-, 2-, 3-, 4-, 5-, 6-spikes. Beyond the 6-spikes, the bursting branch merges with the spiking branch (blue).

The period-adding sequences shown in Figs. 8 and 9 give little insight into why the chaos arises only in MLN. By comparing the top frame of Fig. 11 with the top frame of Fig. 12, however, it becomes apparent why choas arises only in Fig. 12. Chaos does not appear when the bursting branch (pink) is far appart from the spiking branch (blue) as in Fig. 11. Chaos arises only if these two branches are closely spaced as in Fig. 12. That is, chaos is due to SPSs (pink) and UPSs (blue) coexisting in vicinity.

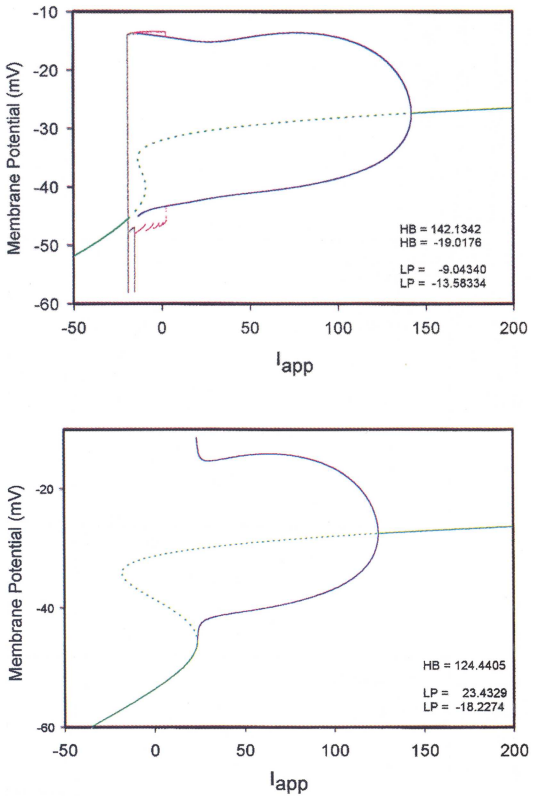

FIGURE 12 AUTO plot for the mollusc neuron. The top frame is plotted using the full equations, and the bottom frame is plotted by fixing p_∞ of I_{crac} at $K_{crac}\cdot/(K_{crac}+50)$. (See Color Plate IV.)

7. PHASE PLANE ANALYSIS

Phase plane analysis is another way of studying why a complex dynamic structure arises from the model under study. This analysis assumes that the multivariables in the model can be reduced to two variables. In the case of the TCN, these variables are the membrane potential (V) and the inactivation variable f of I_{Ca} as shown in Fig. 13. In the case of MLN, these two variables are V and $[Ca^{2+}]_{ER}$ as shown in Fig. 14.

How delta and spiral waves arise as I_{app} is raised can be explained when the dynamic orbital is projected onto the V–f phase plane. On this plane, we superimpose the V-nullcline (green) and the f-nullcline (red). Here, the f-nullcline was obtained from the relation, $f=f_\infty(V)$, whereas the V-nullcline

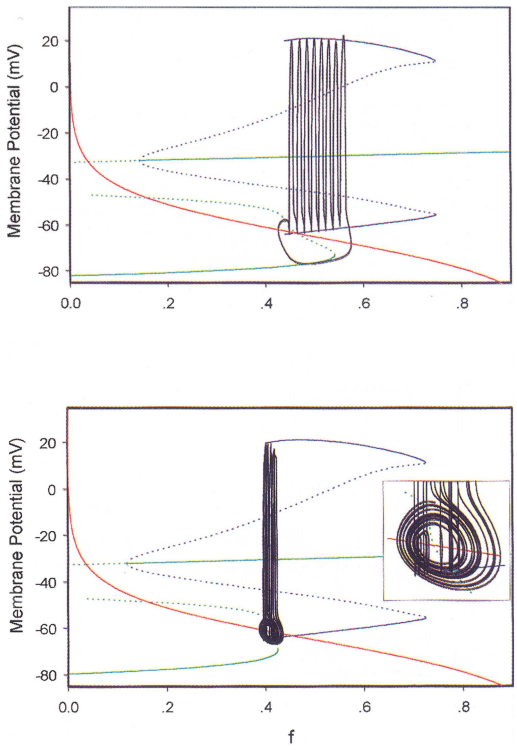

FIGURE 13 The dynamic orbit that travels on the V–f phase plane for the thalamocortical neuron. Here, the red curves are the f-nullclines ($df/dt = 0$), the green curves are the V-nullclines ($dV/dt = 0$), and the blue curves are spiking branches. The solid lines signify stable states, while dashes are unstable states. The top frame was constructed using $I_{app} = -3.5\,\mu A/cm^2$, and the bottom frame using $I_{app} = 2.07\,\mu A/cm^2$. (See Color Plate V.)

was drawn by setting the three fast gatings at their steady state (i.e., $d = d_\infty$, $h = h_\infty$, and $n = n_\infty$) and by using AUTO. In the V-nullcline, the solid green lines are stable, and the dashed lines are unstable. The knee is where SSS becomes USS. A fixed point is the point where two nullclines intersect. Oscillation arises when the fixed point is unstable. The fixed point is unstable when the red line intersects the dashed green line.

How delta and spiral waves arise as I_{app} increases can be explained by studying the dynamic orbital on the V–f phase plane. Oscillation is simple as long as the gating variables, d, h, and n, are at their steady states. In this two-variable (V and f) system, the path that the orbit travels is seen by the upper and lower solid green lines – from the left to the right on the lower branch until it hits the knee and then jumps to the upper branch (from the right to left) until it hits the HB (the point where the green solid line becomes the dashed green).

Bursting arises when these variables become dynamic, i.e., by solving all five dynamic variables using AUTO. When the three variables are turned on, a periodic branch appears (see the blue line) in this phase plane. In the periodic branch (blue line), the dashes are unstable and the solids are stable. The homoclinic orbital (HCO) is the point where the SPS (solid blue) intersects the USS (dashed green). At the HCO, the period becomes infinity.

In the upper frame of Fig. 13 where the hyperpolarization current is strong, the spike is generated as the orbit enters the periodic branch and terminates as it passes HCO. As the spike terminates the orbit drops to the lower branch of SSS. From the point of the drop, the orbit moves to the right. As it passes the knee, the orbit enters SPS, and the spikes are generated again. In the lower frame where the hyperpolarization current is weak, the orbit cannot drop all the way down to the SSS but to the USS near the knee. Note that in this region USS curves gently. Since the USS slopes gently, the orbit can spiral around the fixed point. The amplitude of the spiral grows gradually. When it grows enough the Na^+ current is elicited. Once the Na^+ current is activated, the large-amplitude spike follows.

In the case of MLN, the complex oscillations embedded in the model can be explained by projecting the dynamic orbit on the V–$[Ca^{2+}]_{ER}$ phase plane. Figure 14 reveals the orbit which travels at six different locations of the bifurcation diagrams of Fig. 9. Here, repetitive spiking (turquoise) appears at $I_{app} = 5.0$, doublets at $I_{app} = 3.0$, chaos (green) at $I_{app} = 1.0$, 5-spike bursting (red) at $I_{app} = 0.0$, 2-spike bursting (pink) at $I_{app} = -10$, and 1-spike bursting (blue) at $I_{app} = -18$. The solid lines at the bottom are SSSs, the dashed lines in the middle are USSs, and the solid lines at the top and middle are SPSs. Note that the V-nullcline slides to the left and upward as I_{app}

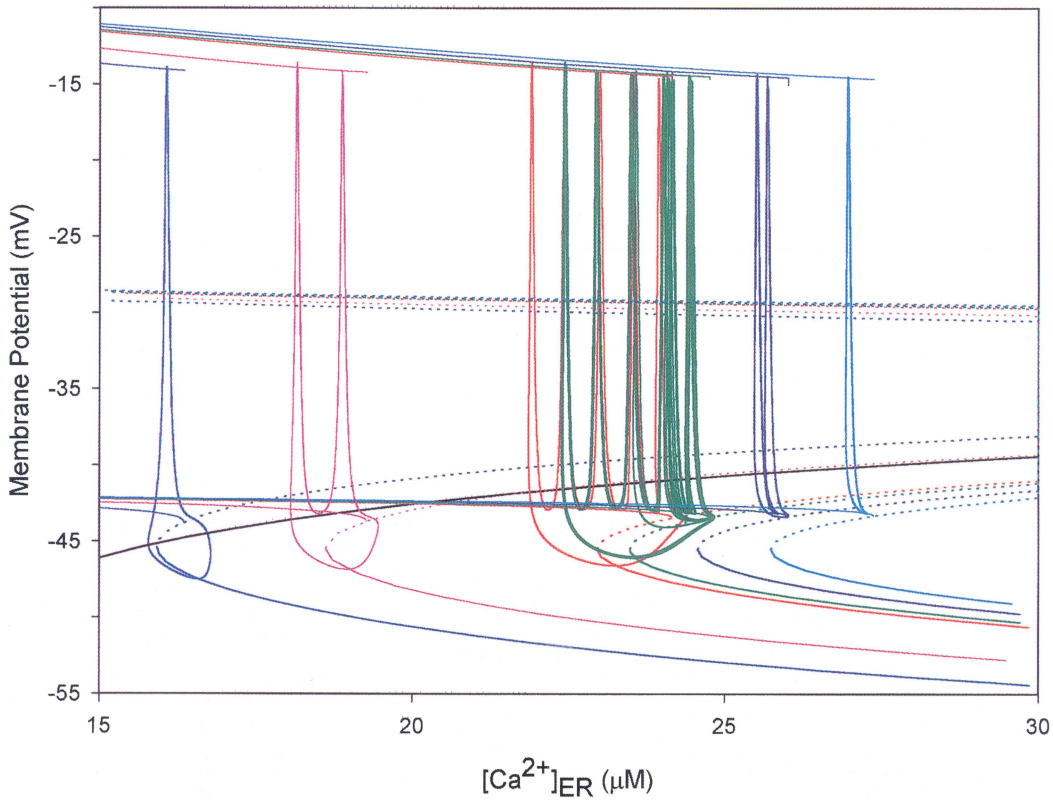

FIGURE 14 The dynamic orbit projected on the V–$[Ca^{2+}]_{ER}$ phase plane for the mollusc neuron at six different I_{app} values: $I_{app} = -18$ (blue), $I_{app} = -10.0$ (pink), $I_{app} = 0.0$ (red), $I_{app} = 1.0$ (green), $I_{app} = 3.0$ (navy blue), and $I_{app} = 5.0\,\mu/cm^2$ (turquoise). Here, the solid lines on the bottom represent SSSs, the dashed lines in the middle represent USSs. The top and middle solid lines are spiking envelopes. (See Color Plate VI.)

increases. The $[Ca^{2+}]_{ER}$-nullcline, on the other hand, is invariant to I_{app} and it intersects the USS (not shown).

How bursting, chaos, and spiking arise from MLN can be explained as follows. Note that the inward current I_{crac} decreases as $[Ca^{2+}]_{ER}$ increases. So, as one moves from the left side to the right, the inward current contributed by I_{crac} decreases, but the inward current contributed by I_{app} increases. Thus, in some regions in the diagram there is an increase in the sum of the two currents, while in others there is a decrease in the sum. A decrease leads to a gain in the downward speed of the orbit, and an increase leads to the opposite effect (i.e., the orbit stays around the periodic branch).

On the left-most region (blue and pink) where I_{app} carries a strong hyperpolarization current, the orbit has a very strong downward speed. This speed sends the orbit to the SSS. Once in the SSS, the orbit moves to the left until it passes the knee. After passing the knee, the orbit enters the SPS, and the spikes are generated. Each time the orbit spikes $[Ca^{2+}]_{ER}$ increases, and this increase results in a decrease of I_{crac}. This decrease causes the spike to come closer and closer to the HCO. As the orbit passes HCO, the spike terminates, and the cycle repeats.

At the right-most region (turquoise and navy blue) where I_{app} carries a sufficiently strong depolarization current, the orbit cannot come

closer to HCO (since it does not have enough downward speed). Repetitive spiking follows.

How does bursting-chaos set in? Follow the green trajectory in Fig. 14. As seen here, if the orbit does not have enough speed to land on the SSS (i.e., the lowest solid line), it gets trapped on the USS (the dashes lines). When the orbit is in the USS, it travels to the left along the path provided by USS. Since this path is unstable the orbit can reenter the SPS in a random manner. One of these entries may cause the orbit to gain enough speed to land on the SSS. Once it lands on the SSS, the orbit has to follow the stable path and enters back to the periodic branch.

8. TYPES OF BIFURCATION DIAGRAMS

The bifurcation diagrams shown in Figs. 10–12 suggest that there are at least four distinct ways that a periodic branch arises from a HB and terminates as I_{app} changes. These structures are schematically presented in Fig. 15.

In Type I, a periodic branch that evolves from one of the HBs terminates when it enters the second HB. An example is seen in the bottom frame of Fig. 10. It also appeared in the two-variable model of Chay and Lee (1990; 1992). A subcritical HB is the HB from which an unstable periodic branch is evolved (as seen in the right HB of top and middle frames in Fig. 10). A supercritical HB is the HB from which a stable periodic state is evolved (as seen in the right HB of the bottom frame of the same figure). For more discussion on types of HB, see Glass and Mackey (1988).

In Type II, a periodic branch evolves from the HB and terminates at a homoclinic orbital giving rise to homoclinic bifurcation (Wang and Rinzel, 1995). When it terminates at the knee it is referred to as saddle node bifurcation. When it terminates at the USS, it is referred to as regular saddle bifurcation. Examples of homoclinic bifurcation

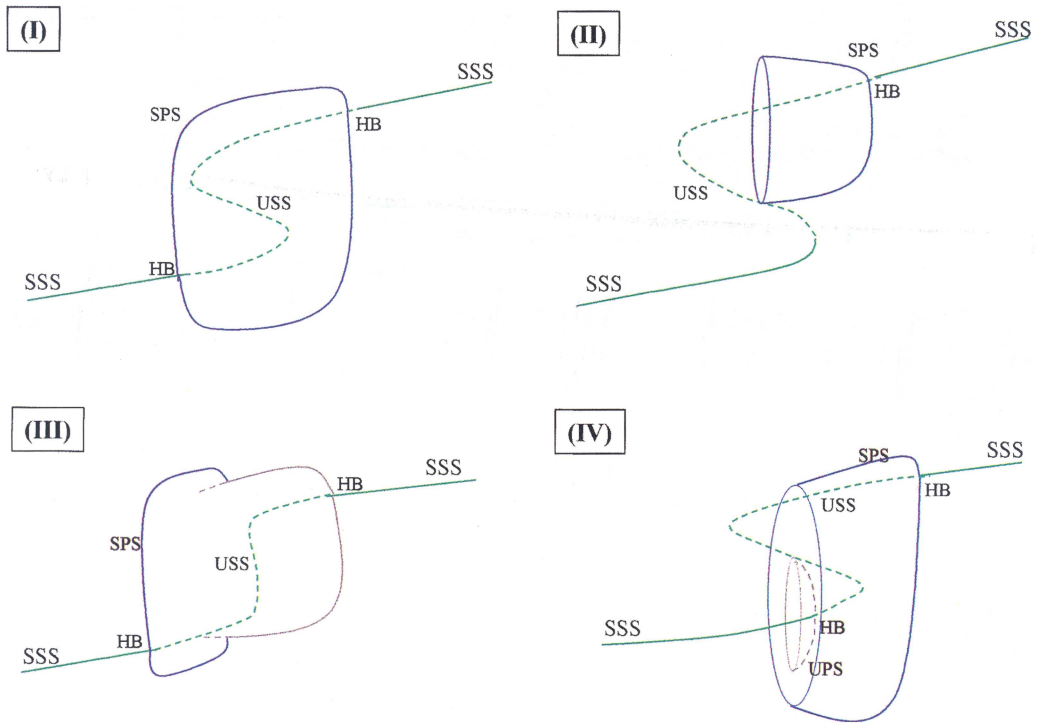

FIGURE 15 Four types of a bifurcation structure, which show how the periodic branch starts and how it ends. (See Color Plate VII.)

are seen in the bottom frames of Figs. 11 and 12. Note in these frames that the periodic state terminates at the knee, forming saddle node bifurcation.

In Type III, a periodic branch that starts from one of HBs terminates with an infinite period when it reaches the USS. Another one that starts from the second HB terminates when it meets the periodic branch from the first HB. An example is shown in the top frame of Fig. 12. Type III has been observed in bursting neurons (see Fig. 5 of Chay *et al.*, 1995). A period-doubling scenario arises from the intersection of the two periodic branches. That is, doublets are formed by SPS and UPS which coexist in this region. The time series of the doublets can be seen in the second trace of Fig. 6, and their phase–plane trajectory can be seen in the navy blue line in Fig. 14.

In Type IV, an unstable periodic branch that is evolved from one of HBs terminates with an infinite period at HCO. Unlike Type II, the amplitude of the oscillation that is evolved from the second HB is so high that it passes the knee. But, this periodic branch also terminates as soon as it passes the first HB. An example is seen in the middle frame of Fig. 10. This has been first observed in the Beeler–Reuter model of ventricular myocardium (Chay and Lee, 1985).

There is another type that is a combination of types III and IV, and this is seen in the left side of the top frames of Figs. 10 and 11. Note from these figures that there are two HBs (left and right). UPS evolves from the left HB and terminates when it meets HCO (as in type IV). However, above this HCO arises a SPS that terminates when it meets a periodic branch from the right HB. This periodic branch can be UPS as in the frame of Fig. 10 or SPS as in the top frame of Fig. 11.

9. NETWORK PHENOMENA

One of the most challenging problems of brain research is how different types of neurons interact so as to give rise to the complex rhythmic behavior seen in the electroencephalograph (EEG) of the brain. Since the brain is too complex, a network behavior can be more effectively studied in other simpler systems, e.g., the islet of Langerhans in pancreas.

The β-cells occupy about 70% of the islet. In the islet, the β-cells are surrounded by at least three other cell types. These are the α-cells that secrete the hormone glucagon, the δ-cells that secrete the hormone somatostatin, and the PP cells that secrete pancreatic polypeptide hormone. Both glucagon and somatostatin affect insulin release such that glucagon enhances the secretion of insulin while somatostatin inhibits the secretion of both insulin and glucagon. In addition, insulin secretion is also affected by neurotransmitters released from both sympathetic and parasympathetic fibers, which enter pancreatic islets.

The α-cells (which lie on the periphery of the islet) have a lower threshold for glucose (i.e., about 5 mM) than β-cells (which require about 7 mM of glucose). How important the role of α-cell is to the β-cell can be seen from experiment of Pipeleers (1984), who showed that intact β-cells (i.e., β-cells in the islet) release 30-fold more insulin than isolated single β-cells. This higher release of insulin by intact β-cells is attributed to glucagon released from the neighboring α-cells (Schuit and Pipeleers, 1985). This is further evidenced by the secretory response which is markedly amplified when single β-cells are incubated in the presence of α-cells or glucagon (Gorus *et al.*, 1984).

The α-cells also affect electrical bursting and $[Ca^{2+}]_i$ oscillation of β-cells. This can be evidenced by Fig. 16 which compares electrical bursting (frames A and C) and $[Ca^{2+}]_i$ oscillation (frames B and C) of single cells (frames A and B) with intact β-cells (frames C and D). The inset of this figure shows electrical bursting (left) and $[Ca^{2+}]_i$ oscillation (right) at the limit cycle. Frame A was retouched from Smith *et al.* (1990), while frames B–D were retouched from Hattori *et al.* (1994). Note that single cells lack what is known as the biphasic response (the rich transient state seen in frames C and D).

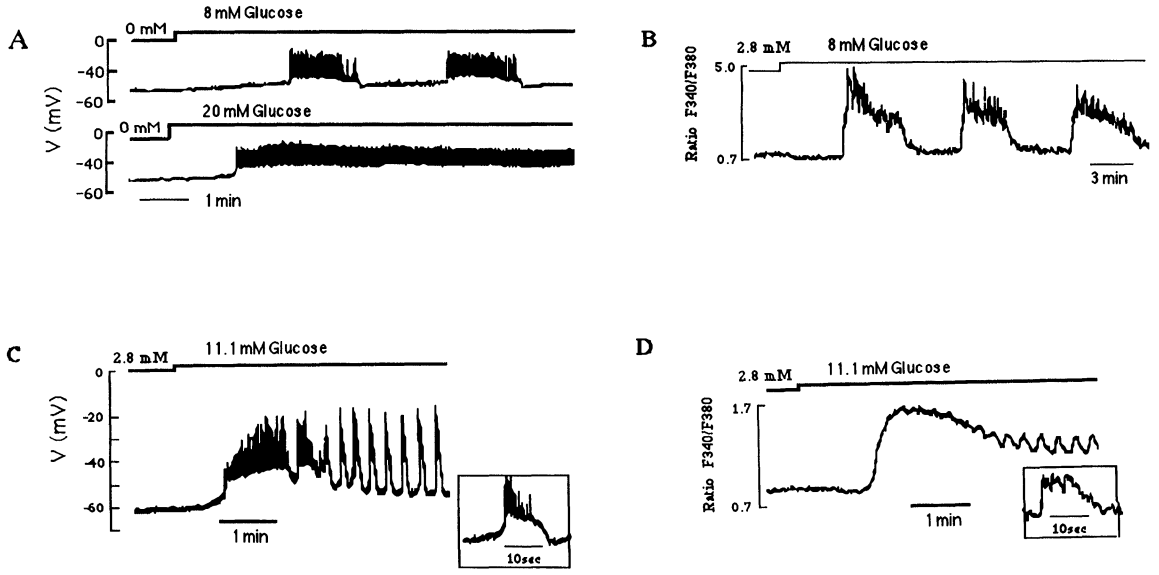

FIGURE 16 Electrical bursting (A) and intracellular calcium oscillation (B) in isolated single β-cells. Electrical bursting (C) and intracellular calcium oscillation (D) in intact β-cells in the islet.

Glucagon and forskolin (an activator of the catalytic subunit of adenylate cyclase) can increase not only the frequency of electrical bursting but also the plateau fraction (the ratio of the activate phase to the silent phase (Ikeuchi and Cook, 1984). Epinephrine and somatostatin, on the other hand, enhance hyperpolarization and decrease the frequency of burst activity (Cook and Perara, 1982; Pace and Tarvin, 1981). This intriguing β-cell bursting behavior is shown in Fig. 17. Note that in the presence of glucagon β-cells burst with a periodicity of several seconds (the top trace), while in the presence of epinephrine the periodicity becomes several minutes (the bottom trace). Insulin production is increased by several-fold in the presence of glucagon, and the opposite is observed in the presence of epinephrine.

The slow bursting (which takes tens of seconds to several minutes) in Figs. 16 and 17 could not possibly be due to a H–H type mechanism, since the H–H mechanism is too fast to generate such slow bursting. Also, it could not be due to the $[Ca^{2+}]_i$ dynamics since this dynamic variable is very fast as evidenced by experiment which shows that it fully grows within tens of milliseconds following the depolarization. To generate such a long periodicity that lasts for tens of seconds to several minutes, the participation of the ER is essential. The ER is not only a slow buffer but also is a store that contains a huge amount of Ca^{2+}.

Based on Figs. 16 and 17 and other experimental evidence, a store-operated mathematical model has been formulated (Chay, 1995; 1996a,b; 1997a,b), which was modified from our previous mathematical β-cell models (Chay, 1985b; 1986; 1987; 1990b,c; 1993a,b; 1996a–c; Chay and Kang, 1988; Chay and Keizer, 1983; Chay *et al.* (1990); Lee *et al.*, 1983). This model is based on the hypothesis that $[Ca^{2+}]_{lum}$ in the ER is a slow dynamic variable and this slow dynamic variable is the origin of the underlying wave in pancreatic β-cell bursting.

The model is schematically presented in Fig. 18. As shown in this figure, three signaling pathways exist in β-cells (Prentki and Matschinsky, 1987): (i) the phosphatidylinositol (PI-) signaling pathway (left) that can activate protein kinase C (PKC), (ii) the glucose-sensing pathway (right) that can activate calcium–calmodulin kinase (Ca–CAM K),

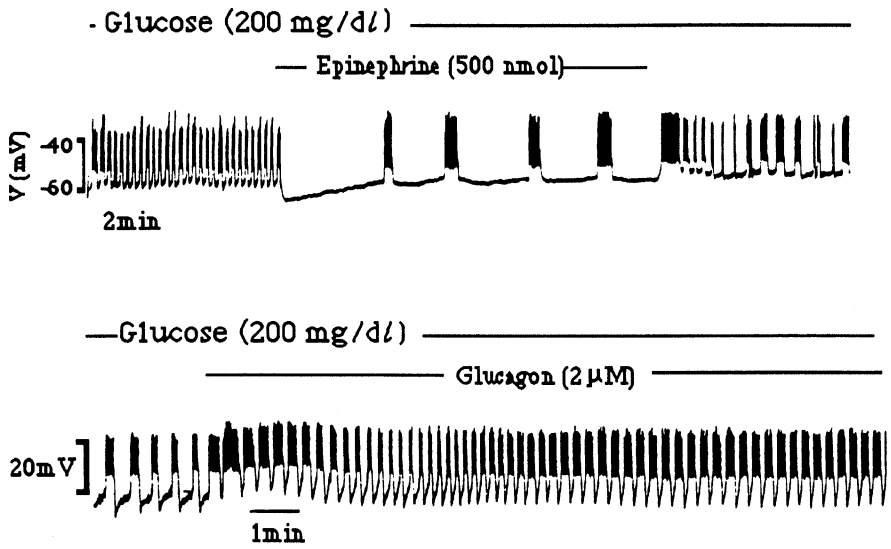

FIGURE 17 Top trace: continuous recording of membrane potential of β-cell exposed to a steady flow of epinephrine (500 nmol) for 15 min. Bottom trace: effect of glucagon (2 mM) on glucose induced electrical activity.

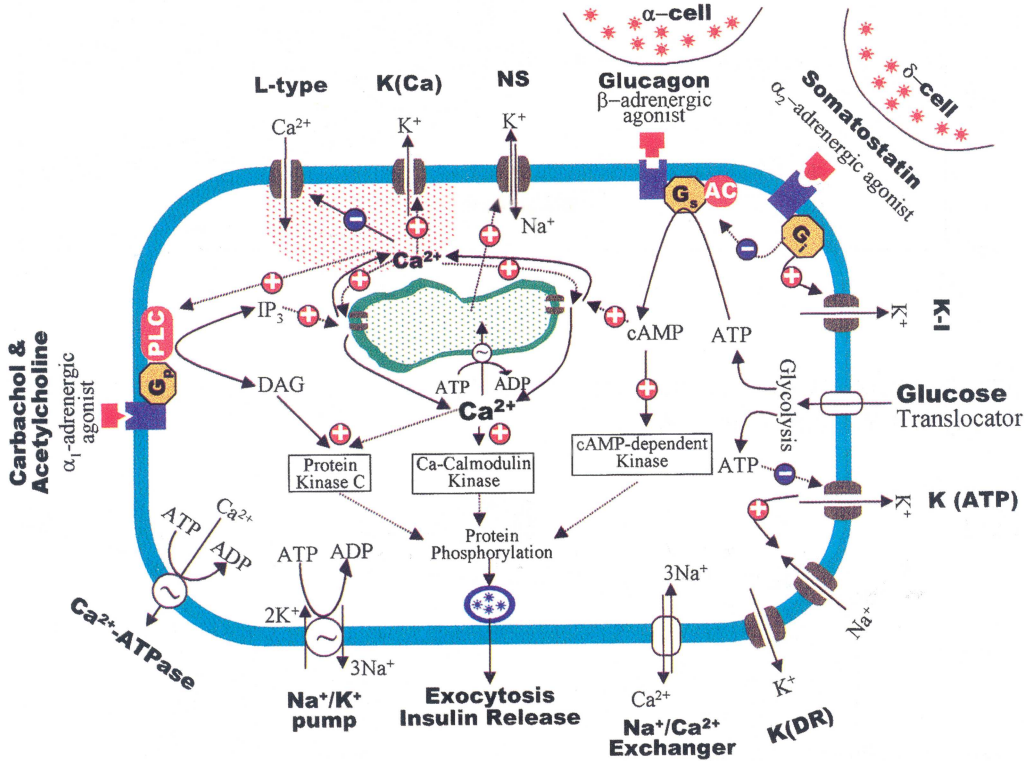

FIGURE 18 Three signaling pathways involved in secretion of insulin from pancreatic β-cells: the phosphatidylinositol-signaling pathway (left), the glucose-pathway (lower right and the center), and the adenylate–cyclase transduction pathway (right). Here, the symbols + and − indicate activation and inhibition, respectively. In the islet of Langerhans, the α-cell secretes glucagon at lower threshold of glucose. (See Color Plate VIII.)

and (iii) the adenylate–cyclase (AC-) transduction pathway (top right) that can activate cyclic AMP-dependent kinase (PKA). These kinases can release insulin from its granules via phosphorylation. An agonist (e.g., neurotransmitters such as acetylcholine or hormones such as glucagon) activates the GTP-bound G-protein when it is bound to their respective receptors (REC). This agonist produces a secondary messenger such as cAMP (see right) and IP_3 (left). When the glucose concentration is raised to about 7 mM, $[ATP]_i$ rises in β-cells, and this rise activates the AC-transduction pathway. How glucagon can raise [cAMP] whereas epinephrine can suppress [cAMP] can be seen from the reactions involved in the right side of Fig. 18

A "hot" spot exists underneath a cluster of L-type Ca^{2+} channels (see the top left). This channel opens when the membrane is depolarized, permitting extracellular Ca^{2+} ions to come inside the cell and inactivates when $[Ca^{2+}]_i$ is undesirably high. A Ca^{2+}-sensitive K^+ channel [K(Ca)] coexists with L-type channels. In the vicinity of the VDCCs lies a voltage-independent non-selective (NS) cationic channel, which is activated when $[Ca^{2+}]_{lum}$ becomes low. Outside this hot spot lies a voltage-dependent delayed rectifying K^+ [DR(K)] channel, which contributes to spike activity.

In the hot spot lie two types of intracellular calcium stores (ICSs): the ER and insulin containing secretory granules (SGs). SGs sequester intracellular Ca^{2+} via its Ca^{2+}-ATPase pump and then release insulin and intragranular Ca^{2+} into the external medium during exocytosis (Bovist *et al.*, 1995). The ER contains a SERCA that pumps intracellular Ca^{2+} into the ER. The ER also contains two types of CRC – an IP_3-sensitive CRC and a ryanodine-sensitive CRC whose activity is modulated by both $[Ca^{2+}]_i$ and cAMP.

According to this model, the K(ATP) is active at rest. The NS channel is also active since the ER is nearly empty. The current generated by these two channels is the main source of the resting potential of -70 mV. Addition of glucose raises $[ATP]_i$. A rise of $[ATP]_i$ triggers several events. First, the K(ATP) channels close (the lower right of Fig. 18). This closure leads to depolarization as seen in frame C of Fig. 16. As the K(ATP) channel closes, a low-threshold transient Na^+ channel of a H–H type is activated first. This channel, in turn, activates a slower voltage-dependent L-type Ca^{2+} channel. Second, SERCA is activated, which in turn decreases $[Ca^{2+}]_i$ as seen in frame D of Fig. 16. Third, a rise of $[ATP]_i$ raises [cAMP] via the AC-signaling pathway (see the reaction on the right of Fig. 18). [cAMP] enhances activity of CRC in the ER. During the transient rich active phase (see Fig. 16C), more intracellular Ca^{2+} is pumped into the ER. When ER is filled sufficiently by Ca^{2+}, the cell repolarizes (due to inactivation of the NS current) as seen in frame C of Fig. 16. Enhanced CRC prevents $[Ca^{2+}]_i$ to come all the way down to the initial level. Biphasicity is a result of enhanced CRC activity.

As shown in Fig. 19, the model exhibits more than a 10-fold increase in the frequency of bursting when k_{rel} (i.e., CRC activity) is increased by 10-fold. This explains why glucagon and somatostatin have the ability to control the frequency of the bursting (see Fig. 17). Note that isolated, single cells lack neighboring α-cells. That explains why isolated β-cells contain a very low concentration of cAMP, and this is why single β-cells burst with a periodicity lasting for several minutes while intact β-cell bursts with a periodicity lasting for tens of seconds (see Fig. 16).

Note from Figs. 16, 17 and 19 that the faster bursting causes a decrease in the amplitude of both electrical bursting and $[Ca^{2+}]_i$ oscillation. Note also that the $[Ca^{2+}]_i$ level becomes higher as the frequency becomes faster. A lot more insulin is secreted from intact β-cells than from isolated β-cells. Likewise, a lot more insulin is secreted from β-cells in the presence of glucagon than epinephrine. This implies that insulin secretion is modulated both by frequency and amplitude (Chay, 1997b). Figure 19, thus, is a demonstration that neighboring glucagon secreting α-cells are required for β-cells to release insulin in an optimal way.

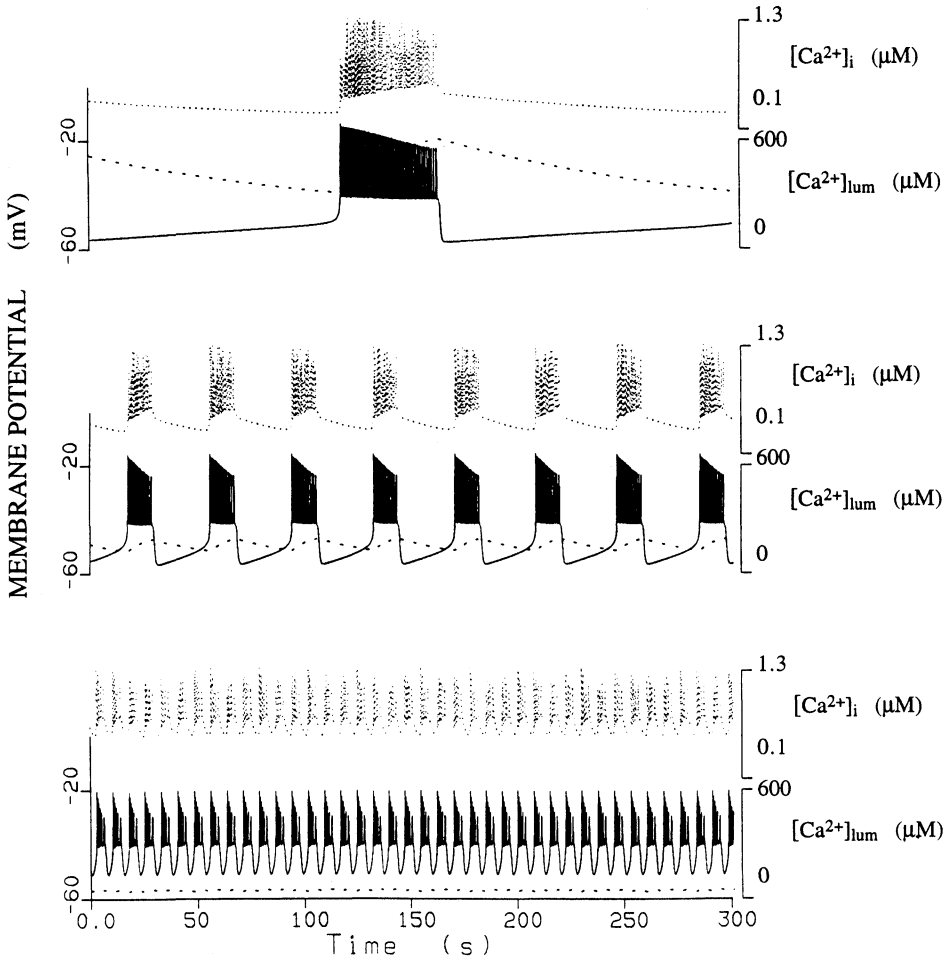

FIGURE 19 Model simulation by changing k_{rel}, the release rate of the calcium releasing channel. The parameter k_{rel} is increased from $0.03\,s^{-1}$ (top), to $0.1\,s^{-1}$ (middle), and to $0.5\,s^{-1}$ (bottom).

10. DISCUSSION

Two types of chaos have been discovered in the models presently reviewed: period-reducing chaos that leads to spindle oscillations (Figs. 7 and 13) and period-adding chaos that leads to an inverse period-doubling sequence (Figs. 9 and 14). In the period-reducing scenario exhibited by TCN (Fig. 7), the spikes are reduced one by one at first. When the spikes are reduced sufficiently chaos appears in the transition region where a spike disappears. The chaotic regime becomes broader and more complex at first, then it becomes narrower and simpler as the spikes disappear one by one until only one spike remains. Beyond the 1-spike bursting, this neuron generates spindle- type chaotic oscillations. In the period-adding scenario exhibited by MLN (Fig. 9), a spike is added, one by one at first. When spikes are sufficiently added, chaos appears in the region where a new spike appears. Crisis transition (Grebogi and Ott, 1983) sets in, and this transition leads to a familiar period-doubling sequence in an inverse order. As one can see in Fig. 8, not all the period-adding sequences contain chaos.

To our knowledge a period-adding scenario was first observed in Chay's neuronal models (1984;

1985a), and a period-reducing scenario was first observed in the Chay–Fan model (1993) and later in Wang's thalamic relay neuron model (1994). In addition to the currents that appear in the Chay–Fan model, Wang's model contains two other currents – a hyperpolarization activated cationic NS current and a persistent Na^+ current that does not inactivate. Since the bursting structure from his model is almost identical to that of the Chay–Fan model, these two currents must be playing submissive roles. In the Chay–Fan model, this submissive current is modeled by $I_{app} = 2.6\,\mu A/cm^2$ at the resting potential of -60 mV.

According to the way the neurons burst, we classify their bursting structures by two ways – fast bursters with a periodicity of a few hundred milliseconds and slow bursters with a periodicity of tens of seconds. In this review, we showed that the slow bursters require the participation of the ER in addition to the ion channels in the plasma membrane and $[Ca^{2+}]_i$ dynamics. Not only does the ER act as a Ca^{2+} buffer (so as to slow down the rhythm), but it also releases luminal Ca^{2+} by a calcium-induced Ca^{2+} release mechanism. The neurotransmitters involved in the PI- and AC-signaling pathways influence the burst periodicity by modulating CRCs in the ER (see Figs. 17 and 19). The faster bursters (e.g., TCN and PYN), on the other hand, do not require the ER participation. These bursters seem to utilize the ER only under unusual circumstances (e.g., coma) by releasing the neurotransmitters/hormones involved in the two signaling pathways.

Our view that there are two classifications for the bursting structure contrasts that of Wang and Rinzel (1995), who classified the bursters according to the ion channels involved in the bursters. The gating kinetics of ion channels are very fast processes which occur within a few hundred milliseconds at most. Therefore, it is not possible that the channel kinetics can generate such slow bursters.

As shown in MLN and β-cells, the ER can also communicate with a "capacitative" channel in the plasma membrane, in that this channel allows extracellular Ca^{2+} to enter the cell when the luminal Ca^{2+} concentration is lowered. This capacitative current may be a voltage-independent Ca^{2+} channel as in MLN or a non-selective cationic channel as in pancreatic β-cells. The latter channel indirectly allows extracellular Ca^{2+} to enter the cell by activating a voltage-dependent Ca^{2+} channel in the plasma membrane.

Bursting cells in the central nervous system and oscillating sinus nodal cells in the heart also utilize a cationic NS current in order to generate rhythms. However, this current known as I_f or I_h is activated by hyperpolarization. This raises a question whether I_f or I_h is also modulated by $[Ca^{2+}]_{ER}$ and the hyperpolarization activation is merely a consequence of the ER modulation. This hypothesis based on the observation that the NS channel in β-cells is indirectly modulated by hyperpolarization, in that $[Ca^{2+}]_{ER}$ becomes low when V becomes hyperpolarized and it becomes high when V is depolarized (Chay, 1996b,c).

Earlier, Traub *et al.* (1991) have formulated a 19-compartment cable model for the pyramidal cells of CA3 and CA1 regions of guinea-pig hippocampus. A network of this model was able to simulate several important aspects of the experimental recordings made on hippocampal slices (Traub *et al.*, 1991; 1992; 1993; 1994). With this multi-compartmental model, we can learn how the soma and dendrites communicate. However, with our one-compartment model we can explore the behavior of a very large network more efficiently. In addition, the one-compartment model will allow us to reformulate the model that is applicable to the pyramidal cells of CA3 and CA1 in more efficient way. Traub *et al.*'s model in current form (and our one-compartment model) is not able to simulate traces c and d of Fig. 1B. The fact that these two models cannot simulate the crucial experimental features of Wong *et al.* (1981) should be taken as an indication that the mechanisms assumed in these models may not even describe the actual events taking place in single pyramidal neurons.

Understanding the cellular mechanisms involved in endogenous rhythms is important in elucidating

how the brain gets various rhythms (e.g., 7–14 Hz spindle waves, 4–7 Hz theta waves, 0.5–4 Hz delta waves, 40 Hz gamma waves) and why it can pervert into abnormal rhythms (e.g., epileptic seizures) under diseased conditions. The study of the brain is complex. In this review, the islet cells of Langerhans is used as an exmaple to gain insights into how a neural net utilizes endogenous rhythm. In the central nervous system, the δ-cells correspond to inhibitory neurons (e.g., the reticular thalamic nucleus) whereas the α-cells correspond to excitatory neurons (e.g., thalamocortical neurons). The bottom trace of Fig. 17 reminds one of the low-amplitude, high-frequency activity in the neocortex characteristic of the awake state, and the top trace reminds of high-amplitude, low-frequncy rhythms during sleep (Steriade *et al.*, 1993).

To gain a deeper understanding of the interaction among islet cells, one should consider the fact that both α- and δ-cells exhibit oscillations in cytosolic Ca^{2+} concentration when they sense glucose (Berts *et al.*, 1996a,b). The oscillatory α- and δ-cells may induce oscillation in cAMP in β-cells. Thus, further studies of interaction among α-, β-, and δ-cells might explain why 30% of β-cells exhibit a mixture of oscillation consisting of slow oscillation of frequency ranging from 0.05 to $0.5\,\mathrm{min}^{-1}$ and superimposed faster oscillations of frequency of about $3\,\mathrm{min}^{-1}$ (Henquin *et al.*, 1982; Cook, 1983; Valdeolmillos *et al.*, 1989).

Constructing a mathematical model that is applicable to real neural nets is a hard task. Even in a single cell level, it requires numerous testing and refining before one can finally produce a mathematical model that can simulate most of the crucial experiments. The study of pancreatic islet offers a way of understanding how various types of the neurons interact to achieve an ideal environment. We have shown that in the islet of Langerhans the neighboring glucagon secreting α-cells are required for insulin secreting β-cells to function effectively (see Figs. 16, 17 and 19). We hope that our effort toward unraveling endogenous rhythm of single neurons and interaction among them will someday lead to clearer understanding of how and why the brain gets various rhythms and how they can pervert into abnormal rhythms under diseased conditions.

Acknowledgment

This work is supported by NSF MCB-9411244 and the Pittsburgh Supercomputing Center through the NIH Division of Research Resources cooperative agreement U41 RR0415.

APPENDIX I: IONIC CURRENTS AND PARAMETERS INVOLVED IN THREE TYPES OF NEURONS

Thalamocortical Neuron

This model is adopted from the model that appeared in Chay and Fan (1993). To be applicable to TCN, we have lowered the potential by $-20\,\mathrm{mV}$ and raised the kinetic parameters by 100. There are four currents in this model:

$$I_{\mathrm{Ca}} = g_{\mathrm{Ca}} df(V - V_{\mathrm{Ca}}), \quad I_{\mathrm{Na}} = g_{\mathrm{Na}} m_\infty^3 h(V - V_{\mathrm{Na}}),$$
$$I_{\mathrm{K}} = g_{\mathrm{K}} n(V - V_{\mathrm{K}}), \quad I_{\mathrm{L}} = g_{\mathrm{L}}(V - V_{\mathrm{L}}).$$

The basic parametric values in the model are as follows: $C_{\mathrm{m}} = 1\,\mu\mathrm{F/cm}^2$, $g_{\mathrm{Ca}} = 1.4\,\mathrm{mS/cm}^2$, $g_{\mathrm{Na}} = 80\,\mathrm{mS/cm}^2$, $g_{\mathrm{K}} = 50\,\mathrm{mS/cm}^2$, $g_{\mathrm{L}} = 2\,\mathrm{mS/cm}^2$, $V_{\mathrm{Ca}} = 130\,\mathrm{mV}$, $V_{\mathrm{Na}} = 70\,\mathrm{mV}$, $V_{\mathrm{K}} = -85\,\mathrm{mV}$, $V_{\mathrm{L}} = -80\,\mathrm{mV}$, $V_d = -60\,\mathrm{mV}$, $S_d = 7\,\mathrm{mV}$, $V_f = -65\,\mathrm{mV}$, $S_f = -10\,\mathrm{mV}$, $V_{\mathrm{m}} = -45\,\mathrm{mV}$, $S_{\mathrm{m}} = 5\,\mathrm{mV}$, $V_h = -60\,\mathrm{mV}$, $S_h = -9\,\mathrm{mV}$, $V_n = 5\,\mathrm{mV}$, $S_n = 15\,\mathrm{mV}$, $\lambda_d^{-1} = 10\,\mathrm{ms}$, $\lambda_f^{-1} = 400\,\mathrm{ms}$, $\lambda_h^{-1} = 2\,\mathrm{ms}$, $\lambda_n^{-1} = 3\,\mathrm{ms}$, $a_h = 0.5$, $a_d = 0.5$, $a_f = 0.5$, $a_n = 0$.

Pyramidal Neurons

This is unpublished work of Chay and Lee. This model contains six currents:

$$I_{\mathrm{Ca}} = g_{\mathrm{Ca}} d^2(V - V_{\mathrm{Ca}}), \quad I_{\mathrm{Na}} = g_{\mathrm{Na}} m_\infty^2 h(V - V_{\mathrm{Na}}),$$
$$I_{\mathrm{K}} = g_{\mathrm{K}} n(V - V_{\mathrm{K}}), \quad I_{\mathrm{L}} = g_{\mathrm{L}}(V - V_{\mathrm{L}}),$$
$$I_{\mathrm{K(Ca)}} = g_{\mathrm{K(Ca)}} p(V - V_{\mathrm{K}}).$$

Here, the gating variables d, h, and n are voltage dependent (and the equations given by Eqs. 2–4 in the text), while p in the Ca^{2+}-sensitive K^+ channel depends on Ca^{2+} such that

$$p_\infty = \frac{[Ca^{2+}]_i}{K_{KC} + [Ca^{2+}]_i}$$

and

$$\tau_{KC} = \lambda_{KC}\left(1 + \frac{[Ca^{2+}]_i}{K_{KC}}\right)^{-1}.$$

The basic parametric values in the model are as follows: $C_m = 3\,\mu F/cm^2$, $g_{Ca} = 10\,mS/cm^2$, $g_{Na} = 20\,mS/cm^2$, $g_K = 15\,mS/cm^2$, $g_L = 0.2\,mS/cm^2$, $V_{Ca} = 100\,mV$, $V_{Na} = 40\,mV$, $V_K = -75\,mV$, $V_L = -60\,mV$, $V_d = -20\,mV$, $S_d = 9\,mV$, $V_m = -35\,mV$, $S_m = 7.5\,mV$, $V_h = -40\,mV$, $S_h = -4\,mV$, $V_n = -18\,mV$, $S_n = 7.5\,mV$, $\lambda_d^{-1} = 5\,ms$, $\lambda_h^{-1} = 15\,ms$, $\lambda_n^{-1} = 9\,ms$, $\lambda_{KC}^{-1} = 800\,ms$, $a_h = 0.5$, $a_d = 0.5$, $a_n = 0.5$, $K_{KC} = 50\,\mu M$, $\phi = 0.13$, $k_{Ca} = 0.01\,ms^{-1}$, and $[Ca^{2+}]_r = 0.1\,\mu M$.

Molluse Neurons

This model has appeared in Chay (1996a). The model contains the following four currents:

$$I_{Ca} = g_{Ca} d_\infty^3 f(V - V_{Ca}), \qquad I_K = g_K n^4 (V - V_K),$$
$$I_L = g_L (V - V_L), \qquad I_{crac} = g_{crac}\, p_\infty (V - V_K).$$

Here, the gating variables, d, f, and n follows Eqs. (2) and (3) in the text, and p_∞ in $I_{K(Ca)}$ is expressed as

$$p_\infty = \frac{K_{crac}}{K_{crac} + [Ca^{2+}]_{ER}}.$$

The reversal potential V_{Ca} takes a Nernst potential of the following form:

$$V_{Ca} = \frac{RT}{2F} \ln \frac{[Ca^{2+}]_o}{[Ca^{2+}]_i},$$

where $[Ca^{2+}]_o$ is the extracellular calcium concentration.

The basic parametric values in the model are as follows: $C_m = 1\,\mu F/cm^2$, $g_{Ca} = 600\,\mu S/cm^2$, $g_k = 500\,\mu S/cm^2$, $g_L = 6\,\mu S/cm^2$, $g_{crac} = 1.5\,\mu S/cm^2$, $V_k = -75\,mV$, $V_L = -60\,mV$, $V_d = -25\,mV$, $S_d = 9\,mV$, $V_f = -47\,mV$, $S_f = -7\,mV$, $V_n = -18\,mV$, $S_n = 14\,mV$, $\lambda_f = 16\,s^{-1}$, $\lambda_n = 25\,s^{-1}$, $a_f = 0.5$, $a_n = 0$, $K_{crac} = 7\,\mu M$, $K_p = 1.0\,\mu M$, $K_r = 0.5\,\mu M$, $k_{Ca} = 5.0\,s^{-1}$, $k_{pump} = 30\,s^{-1}$, $k_{rel} = 0.3\,s^{-1}$, $\phi = 0.02$, $\rho = 0.2$, $[Ca^{2+}]_r = 0$, $[Ca^{2+}]_o = 2.5\,mM$, and $T = 37°C$.

APPENDIX II: PANCREATIC β-CELL MODEL

This model appeared in Chay (1997). It consists of the following two differential equations:

$$\frac{d[Ca^{2+}]_i}{dt} = -\phi I_{Ca} - k_{Ca}[Ca^{2+}]_i + k_{rel}([Ca^{2+}]_{lum} - [Ca^{2+}]_i) - k_{pump}[Ca^{2+}]_i,$$

$$\frac{d[Ca^{2+}]_{lum}}{dt} = -k_{rel}([Ca^{2+}]_{lum} - [Ca^{2+}]_i) + k_{pump}[Ca^{2+}]_i.$$

There are seven ionic components as shown below:

$$I_{Na} = g_{Na} m_\infty^3 h (V - V_{Na}),$$

$$I_{Ca} = p_{Ca} d f_\infty \frac{2FV}{RT} \times \left\{\frac{[Ca^{2+}]_o - [Ca^{2+}]_i \exp((2FV)/(RT))}{1 - \exp((2FV)/(RT))}\right\},$$

$$f_\infty = \frac{K_{Ca}}{K_{Ca} + [Ca^{2+}]_i},$$

$$I_{NS} = \bar{g}_{NS} \frac{K_{NS}^2}{K_{NS}^2 + [Ca^{2+}]_{lum}^2} \times \left(\frac{V - V_{NS}}{1 - \exp(0.1(V_{NS} - V))} - 10\right),$$

$$I_{K(DR)} = g_{K(DR)} n^4 (V - V_K),$$

$$I_{K(Ca)} = g_{K(Ca)} \frac{[Ca^{2+}]_i^3}{K_{Ca}^3 + [Ca^{2+}]_i^3} (V - V_K);,$$

$$I_{K(ATP)} = g_{K(ATP)} (V - V_K),$$

$$I_L = g_L (V - V_L).$$

The gating variables, d, f, and n follow Eqs. (2) and (3) in the text. The basic parametric values in the model are as follows: $C_m = 1\,\mu F/cm^2$, $g_{Na} = 600\,\mu S/cm^2$, $p_{Ca} = 2.0\,nA/cm^2$, $g_{K(DR)} = 600\,\mu S/cm^2$, $g_{K(Ca)} = 5.0\,\mu S/cm^2$, $g_{NS} = 5.0\,\mu S/cm^2$, $g_{K(ATP)} = 2.0\,\mu S/cm^2$, $g_L = 0.3\,\mu S/cm^2$, $V_{Na} = 80\,mV$, $V_K = -75\,mV$, $V_{NS} = -20\,mV$, $V_L = 80\,mV$, $V_m = -20\,mV$, $S_m = 9\,mV$, $V_h = -48\,mV$, $S_h = -7\,mV$, $V_d = -10\,mV$, $S_d = 5\,mV$, $V_n = 18\,mV$, $S_n = 14\,mV$, $\lambda_h^{-1} = 0.08\,s^{-1}$, $\lambda_d^{-1} = 0.4\,s$, $\lambda_n^{-1} = 0.08\,s$, $a_h = 0.5$, $a_d = 0.5$, $a_n = 0.5$, $K_{Ca} = 1.0\,\mu M$, $K_{NS} = 50\,\mu M$, $k_{Ca} = 7.0\,s^{-1}$, $k_{pump} = 30\,s^{-1}$, $k_{rel} = 0.2\,s^{-1}$, $f = 0.2$, $[Ca^{2+}]_o = 2500\,\mu M$, and $T = 37°C$.

References

Berridge, M.J. (1991). Cytoplasmic calcium oscillations: A two pool model. *Cell Calcium* **12**: 63–72.

Berts, A., Ball, A., Dryselius, S., Glyfe, E. and Hellman, G. (1996a). Glucose stimulation of somatostatin-producing islet cells involves oscillatory Ca^{2+} signalling. *Endocrinology* **137**: 693–697.

Berts, A., Ball, A., Glyfe, E. and Hellman, G. (1996b). Suppression of Ca^{2+} oscillations in glucagon producing a_2-cells by insulin/glucose and amino acid. *Biochim. Biophys. Acta* **1310**: 212–216.

Bovist, K., Eliasson, L., Ammala, C., Renstron, E. and Rorsman, P. (1995). Co-localization of L-type Ca^{2+} channels and insulin-containing secretory granules and its significance for the initiation of exocytosis in mouse pancreatic β-cells. *EMBO J.* **14**: 50–57.

Chay, T.R. (1983). Eyring rate theory in excitable membranes: Application to neuronal oscillations. *J. Phys. Chem.* **87**: 2935–2940.

Chay, T.R. (1984). Abnormal discharges and chaos in a neuronal model system. *Biol. Cyber.* **52**: 301–311.

Chay, T.R. (1985a). Chaos in a three-variable excitable cell model. *Physica D* **16**: 233–242.

Chay, T.R. (1985b). Glucose response to bursting-spiking pancreatic β-cells by a barrier kinetic model. *Biol. Cybern.* **52**: 339–349.

Chay, T.R. (1986). On the effect of the intracellular calcium-sensitive K^+ channel in the bursting pancreatic β-cells. *Biophys. J.* **50**: 765–777.

Chay, T.R. (1987). The effect of inactivation of calcium channels by intracellular Ca^{2+} ions in the bursting pancreatic β-cells. *Cell Biophys.* **11**: 77–90.

Chay, T.R. (1990a). Bursting excitable cell models by inactivation of Ca^{2+} currents. *J. Theor. Biol.* **142**: 305–315.

Chay, T.R. (1990b) Electrical bursting and intracellular Ca^{2+} oscillations in excitable cell models. *Biol. Cybernetics* **63**: 15–23.

Chay, T.R. (1990c) The effect of compartmentalized Ca^{2+} ions on electrical bursting activity of pancreatic β-cells. *Am. J. Physiol.* **258** (*Cell Physiol.* **27**): C55–C965.

Chay, T.R. (1993a). Modelling for nonlinear dynamical processes in biology. In: *Patterns, Information and Chaos in Neuronal Systems*, B.J. West, Ed. World Scientific Publishing, River Edge, NJ, pp. 73–122.

Chay, T.R. (1993b). Modelling pancreatic β-cell electrical activity and insulin secretion. *Adv. Biophys.* **29**: 75–103.

Chay, T.R. (1995). Bursting, spiking, and chaos in an excitable cell model: The role of an intracellular calcium store. *Proc. NOLTA'95* **2**: 1049–1052.

Chay, T.R. (1996a). Modeling slowly bursting neurons via intracellular calcium stores and voltage-independent calcium current. *Neural Comp.* **8**: 951–978.

Chay, T.R. (1996b). Electrical bursting and luminal calcium oscillation in excitable cell models. *Biol. Cyber.* **75**: 419–431.

Chay, T.R. (1996c). The role of endoplasmic reticulum in genesis of complex oscillations in pancreatic β-cells. *IEICE Trans. Fundamentals* **E79-A**: 1565–1600.

Chay, T.R. (1997a). Effects of extracellular calcium on electrical bursting and intracellular and luminal calcium oscillations in insulin secreting pancreatic β-cells. *Biophys. J.* **73**: 1673–1688.

Chay, T.R. (1997b). Why do pancreatic β-cells burst? A hypothesis on frequency encoding by a calcium store. *Proc. Second World Congress of Nonlinear analysts WCNA96. Nonlinear Analysis* **30**(2): 961–972.

Chay, T.R. and Fan, Y.S. (1993). Evolution of periodic states and chaos in two types of neuronal models. In: *Chaos in Biology and Medicine*, W.L. Ditto, Ed. *Proc. SPIE* **2036**: 100–114.

Chay, T.R. and Cook, D.L. (1988). Endogenous bursting patterns in excitable cells. *Math. Biosci.* **90**: 139–153.

Chay, T.R. and Lee, Y.S. (1985). Phase resetting and bifurcation in the ventricular myocardium. *Biophys. J.* **47**: 641–651.

Chay, T.R. and Lee, Y.S. (1990). Bursting, beating, and chaos by two functionally distinct inward current inactivations in excitable cells. *Ann. N.Y. Acad. Sci.* **591**: 328–350.

Chay, T.R. and Lee, Y.S. (1992). Studies on reentrant arrhythmias and ectopic beats in excitable tissues by bifurcation analysis. *J. Theor. Biol.* **155**: 137–171.

Chay, T.R. and Kang, H.S. (1988). Role of single-channel stochastic noise in bursting clusters of pancreatic β-cells. *Biophys. J.* **54**: 427–435.

Chay, T.R., Kim, J.R. and Cook, D. (1990). The effect of ATP-sensitive K^+ channels on the electrical burst activity and insulin secretion in pancreatic β-cells. *Cell Biophys.* **17**: 11–36.

Chay, T.R. and Rinzel, J. (1993). Bursting, beating, and chaos in an excitable membrane model. In: *Biological Physics*. E.V. Mielczarek, E. Greenbaum and R.S. Kox, Eds. American Institute of Physics. New York, pp. 236–245.

Chay, T.R., Fan, Y.S. and Lee, Y.S. (1995). Bursting, spiking, chaos, fractals, and universality in biological rhythms. *Int. J. Bifurc. Chaos* **5**: 595–635.

Cook, D. (1983). Isolated islets of Langerhan have slow oscillations of electrical activity. *Metabolism* **32**: 681–685.

Cook, D.L. and Perara, E. (1982). Islet electrical pacemaker response to alpha-adrenergic stimulation. *Diabetes* **31**: 985–990.

Destexhe, A., Babloyantz, A. and Sejnowski, T.J. (1993a). Ionic mechanisms for intrinsic slow oscillations in thalamic relay neurons. *Biophys. J.* **65**: 1538–1552.

Destexhe, A., McCormick, D.A. and Sejnowski, T.J. (1993b). A model for 8–10 Hz spindling in interconnected thalamic relay and reticularis neurons. *Biophy. J.* **65**: 2473–2477.

Doedel, E. (1981). AUTO: A program for the automatic bifurcation analysis of autonomous systems. *Cong. Num.* **30**: 265–284.

Doedel, E. and Kernevez, J.P. (1986). AUTO: Software for continuation and bifurcation problems in ordinary differential

equation. Applied Mathematics Report, California Institute of Technology.

Doedel, E., Keller, H.B. and Kernevez, J.P. (1991a). Numerical analysis and control of bifurcation problems (I) bifurcation in finite dimensions. *Inter. J. Bifur. Chaos* **1**: 493–520.

Doedel, E., Keller, H.B. and Kernevez, J.P. (1991b). Numerical analysis and control of bifurcation problems (I) bifurcation in infinite dimensions. *Inter. J. Bifurc. Chaos* **1**: 745–772.

Doedel, E.J., Champneys, A.R., Fairgrieve, T.F., Kuznetsov, Yuri A., Sandstede, B. and Wang, X.J. AUTO97: Continuation and bifurcation software for ordinary differential equations, available from ftp.cs.concordia.ca. directory pub/doedel/auto, 1997.

Glass, L. and Mackey, M. (1988). *From Clocks to Chaos, The Rhythms of Life*. Princeton University Press, Princeton, NJ.

Gorus, F.K., Malaisse, W.J. and Pipeleers, D.G. (1984). Differences in glucose handling by pancreatic A- and B-cells. *J. Biol. Chem.* **25**: 1196–1200.

Grebogi, C. and Ott, E. (1983). Crisis, sudden changes in chaotic attractors, and transient chaos. *Physica D* **7**: 181–200.

Feigenbaum, M.J. (1983). Universality in nonlinear systems. *Physica D* **7**: 16–39.

Hattori, M., Kai, R. and Kitassato, H. (1994). Effects of lowering external Na^+ concentration on cytoplasmic pH and Ca^{2+} concentration in mouse pancreatic β-cells: Mechanism of periodicity of spike-bursts. *Jap. J. Physiol.* **44**: 283–292.

Henquin, J.-C., Meissner, H.P. and Schmeer, W. (1982). Cyclic variations of glucose-induced electrical activity in pancreatic B cells. *Pflugers Arch.* **393**: 322–327.

Himmel, D.M. and Chay, T.R. (1987). Theoretical studies on the electrical activity of pancreatic β-cells as a function of glucose. *Biophys. J.* **51**: 89–107.

Hodgkin, A. and Huxley, A.F. (1952). A quantitative description of membrane current and application to conduction and excitation in nerve. *J. Physiol. (London)* **117**: 500–544.

Hoth, M. and Penner, R. (1992). Depletion of intracellular calcium stores activates a calcium current in mast cells. *Nature* **355**: 353.

Lee, Y.S., Chay, T.R. and Ree, T. (1983). On the mechanism of spiking and bursting in excitable cells. *J. Biophys. Chem.* **18**: 25–34.

Lotshaw, D.P., Levitan, E.S. and Levitan, I.B. (1986). Fine tuning of neuronal electrical activity: Modulation of several ion channels by intracellular messengers in a single identified nerve cell. *J. Exp. Biol.* **124**: 307–322.

McCormick, D.A. (1992). Neurotransmitter actions in the thalamus and cerebral cortex and their role in neuromodulation of thalamocortical activity. *Prog. Neurobiol.* **39**: 337–388.

Nunez, A., Curro Dossi, R., Contreras, D. and Steriade, M. (1992). Intracellular evidence for incompatibility between spindle and delta oscillations in thalamocortical neurons of cat. *Neurosci.* **48**: 75–85.

Pace, C.S. and Tarvin, J.T. (1981). Somatostatin: mechanism of action in pancreatic islet β-cells. *Diabetes* **30**: 836–842.

Pipeleers, D. (1984). Islet cell interactions with pancreatic B-cell. *Experientia* **40**: 1114–1125.

Plant, R.E. (1981). Bifurcation and resonance in a model for bursting nerve cells. *J. Math. Biol.* **11**: 15–32.

Prentki, M. and Matschinsky, F.M. (1987). Ca^{2+}, cAMP, and phospholipid-derived messengers in coupling mechanisms of insulin secretion. *Physiol. Rev.* **67**: 1185–1248.

Schuit, F.C. and Pipeleers, D.G. (1985). Regulation of adenosine 3′,5′ monophosphate levels in the pancreatic β-cells. *Endocrionology* **117**: 834–840.

Smith, P.A., Ashcroft, F.M. and Rorsman, P. (1990). Simultaneous recordings of glucose dependent electrical activity and ATP-regulated K^+-currents in isolated mouse pancreatic β-cells. *FEBS Lett.* **261**: 187–190.

Steriade, M. and Llinas, R. (1988). The functional states of the thalamus and the associated neuronal interplay. *Physiol. Rev.* **68**: 649–741.

Steriade, M. and McCormick, D.A. and Sejnowski, T.J. (1993). Cellular mechanisms of a synchronized oscillation in the thalmus. *Science* **261**: 361–364.

Traub, R.D., Jefferys, J.G.R. and Whittington, M.A. (1994). Enhanced NMDA conductance can account for eiileptiform activity induced by low Mg^{2+} in the rat hippocampal slice. *J. Physiol.* **478**: 379–393.

Traub, R.D., Miles, R. and Buzsaki, G. (1992). Computer simulation of carbachol-driven rhythmic population oscillation in teh CA3 region of the *in vitro* rat hippocampus. *J. Physiol.* **451**: 653–672.

Traub, R.D., Miles, R. and Jefferys, J.G. (1993). Synaptic and intrinsic conductances shape picrotoxininduced synchronized after-discharges in the guinea-pig hippocampal slice. *J. Physiol.* **461**: 525–547.

Traub, R.D., Wong, R.K.S., Miles, R. and Michelson, H. (1991). A model of a CA3 hippocampal pyramidal neuron incorporating voltage-clump data on intrinsic conductances. *J. Neurophysiol.* **66**: 635–650.

Valdeolmillos, M., Santos, R.M., Contreras, D., Soria, B. and Rosario, L.M. (1989). Glucose-induced oscillations of intracellular Ca^{2+} concentration resembling bursting electrical activity in single mouse islets of Langerhans. *FEBS Lett.* **259**: 19–23.

Wang, X.-J. and Rinzel, J. (1995). Oscillatory and bursting properties of neurons. In: *Atlas of the Brain*. El-Syed, Ed., pp. 686–691.

Wang, X.-J. (1994). Multiple dynamical modes of thalamic relay neurons: Rhythmic bursting and intermitten phase-locking. *Neuroscience* **59**: 21–31.

Wong, R.K.S. and Prince, D.A. (1981). Afterpotential generation in hippocampal Pyramidal cells. *J. Neurophysiol.* **45**: 86–97.